

In-Situ Stress Measurements and Stress Accumulation Level Analysis of Coal Mines in Northern Ordos Basin

Donghui Yang (✉ ydhname@163.com)

Shanxi Datong University <https://orcid.org/0000-0002-2446-1050>

Zhangxuan Ning

Shanxi Datong University

Yongming Li

Shanxi Datong University

Zhaoheng Lv

Shanxi Datong University

Yuandong Qiao

Shanxi Datong University

Research

Keywords: In situ stress, Kaiser effect, Drilling core, Paleomagnetic technology, Stress accumulation level

Posted Date: November 24th, 2020

DOI: <https://doi.org/10.21203/rs.3.rs-111737/v1>

License:  This work is licensed under a Creative Commons Attribution 4.0 International License.

[Read Full License](#)

Version of Record: A version of this preprint was published on February 7th, 2021. See the published version at <https://doi.org/10.1007/s40789-021-00407-7>.

In-situ stress measurements and stress accumulation level analysis of coal mines in northern Ordos Basin

Donghui Yang*, Zhangxuan Ning, Yongming Li, Zhaocheng Lv, Yuandong Qiao

School of Coal Engineering, Shanxi Datong University, Datong 037003, China

6 Highlights

- For rock masses around 350m, k tends to 1 and the mines enter a critically deep state
 - The principal stresses tested by KE have error about 15% with that of OC, ASR, and HF
 - σ_H dominant orientation is basically consistent with that of focal mechanism solution
 - The fracture stress of mines is lower than friction limit state, and its level is low

11 Abstract

12 For non-directional drilling cores, the sample selection and test method for Kaiser effect (KE)
 13 in-situ stress measurement were proposed, and the magnitude and direction of its principal
 14 stresses were theoretically derived. Based on this method, the KE of 423 samples in Burtai and
 15 Baode coal mines in northern Ordos Basin (NOB) were tested. The results show that σ_H , σ_h and
 16 σ_v vary with depth and location, and their values increase with increasing of depths. Generally,
 17 horizontal stresses play a leading role. There are main stress regimes in NOB: $\sigma_H > \sigma_h > \sigma_v$
 18 (Burtai, <172m; Baode, <170m) and $\sigma_H > \sigma_v > \sigma_h$ (Burtai, 170-800 m; Baode, 170-400 m), and
 19 the $\sigma_v > \sigma_H > \sigma_h$ stress regime is mainly distributed in moderately deep to deep coal mines. For
 20 rock masses with a depth of 350m, $k ((\sigma_H + \sigma_h) / 2\sigma_v)$ tends to 1, indicating that deep critical
 21 state will gradually emerge. The test results were compared with those of overcoring method
 22 (OC), elastic strain recovery (ASR) and micro-hydraulic fracturing (HF). The relative errors of
 23 σ_H , σ_h and σ_v are 14.90%, 19.67%, 15.47% (Burtai) and 10.74%, 22.76%, 19.97% (Baode), and
 24 they are all within a reasonable range required by the project, which verifies the reliability of
 25 KE method. The dominant orientation of σ_H (Burtai, NE-NNE; Baode, NEE) was obtained by
 26 using paleomagnetic technology, which is consistent with that (NE-NEE) of earthquake focal

27 mechanisms in this area. Based on Byerlee-Anderson theory, the stress accumulation level of
28 mine rock mass was discussed. Under dry rocks or hydrostatic pressure rocks, the friction
29 coefficient of faults is both low, which is less than the lower limit (0.6) of strike-slip faults slip,
30 indicating that the fracture stress with a low level around the study area is lower than the friction
31 limit stress. The stress accumulation level in Baode mine is slightly larger than that in Burtai
32 mine.

33 **Keywords:** In situ stress; Kaiser effect; Drilling core; Paleomagnetic technology; Stress
34 accumulation level

35 **1. Introduction**

36 In the long process of geological evolution, the crustal rock mass is continuously adjusted
37 and evolved under the coupling of water and rock corrosion, pressure dissolution, high-
38 temperature thermal stress, and long-term creep, resulting in the in-situ stress distribution with
39 time-space complexity and variability. It is not only the key factor to determine the stability of
40 the regional structure, but also an important force source to affect the stability of roadways
41 such as mining engineering ([Yuan, 2017](#); [Qian, 2012](#)). With the increase of demand for energy
42 and mineral resources and the increase of mining intensity, deep environment mining has been
43 carried out successively. There are problems such as "three highs and one disturbance" of high
44 in-situ stress, high in situ temperature, high water pressure and strong mining disturbance,
45 which will become the focus and difficulty in deep mining rock mechanics and engineering
46 ([Xie et al., 2015](#)). Accurately obtaining the distribution and accumulation level of in-situ stress
47 is the way to solve the above problems.

48 Since 1932, [Lieurace \(1933\)](#) took the lead in testing the surrounding rock stress in spillway
49 tunnel with the method of surface stress relief at the bottom of Hoover Dam, Since then, in-
50 situ stress testing technology has developed rapidly, and it has been widely used in many fields,
51 such as energy utilization of oil, gas, water, geothermal, resource development of coal mines,
52 metal mines, earthquake prediction, nuclear waste disposal, and so on ([Su, 2002](#)). So far, there
53 are dozens of in-situ stress testing methods, but no unified classification standard has been
54 formed. They can be classified according to data sources and can be roughly divided into five

55 categories: core-based methods, borehole-based methods, geological methods, underground
56 space-based methods and geophysical methods (seismological methods) ([Zang and](#)
57 [Stephansson, 2013](#); [Wang, 2014](#); [Stephansson and Brown, 2015](#)). However, different test
58 methods reveal different scales of stress information, and the scope of application is also
59 different. Therefore, several methods need to be used jointly, which are complementary to each
60 other, and finally determine the stress state of the rock mass, to reduce the error caused by
61 different scales of stress information.

62 The development of acoustic emission (AE) monitoring system has created conditions for
63 the accurate identification of the Kaiser effect (KE) and its application. Since Kaiser discovered
64 KE phenomenon in 1957 ([Michihiro et al., 1985](#)), the KE of sandstone and crystalline rock was
65 first confirmed by [Goodman \(1963\)](#), [Kurita and Fujii \(1979\)](#), and most show good KE, such as
66 marble, gneiss, granite, gabbro, greenstone, porphyry, chalcopyrite, and so on, except Kiruna
67 magnetite ([Holcomb, 1983](#); [Li and Nordlund, 1993](#)). Then [Kanagawa et al. \(1976\)](#) first tried to
68 apply KE to in-situ stress test. To obtain the exact KE point, the uniaxial double cyclic loading
69 mode was proposed ([Yoshikawa and Mogi, \(1989\)](#)), and the cyclic peak load (σ_P) must be
70 higher than the estimated previous maximum stress (σ_{Hmax}), and σ_P is 30%–80% of the uniaxial
71 compressive strength (σ_C). At the same time, the deformation rate analysis method (DRA) for
72 testing in-situ stress was proposed. The principle of AE-DRA combined method has been
73 described, the AE method and the DRA method have been mutually confirmed, and the vertical
74 stress of siliceous slate in metal mines ([Xie et al., 2010](#)) and gypsum rock ([Ge et al., 2015](#)) has
75 been determined. Although the mechanism of KE has not been completely solved, the method
76 can meet the engineering needs by comparing the results of KE test and field measurement
77 ([Qin et al., 1993](#)). At present, KE research is mainly focused on hard magmatic rock,
78 metamorphic rock and sedimentary rock, while systematic on coal measures sedimentary rock
79 is less.

80 When the main stress state is $\sigma_H > \sigma_h > \sigma_v$, $\sigma_H > \sigma_v > \sigma_h$ and $\sigma_v > \sigma_H > \sigma_h$, it is conducive
81 to the activities of reverse fault, strike-slip fault and normal fault ([Anderson, 1942](#); [Byerlee,](#)
82 [1978](#)). The change of in-situ stress value around the fault is complex. The HF test results of
83 nearly 1,000 fault block oil wells around the normal and inverse fault areas show that σ_h is
84 parallel to the fault trace ([Sun and Zhang, 2004](#)). According to Mohr-Coulomb criterion ([Hoek](#)

85 [and Brown, 2019](#)), when $\tau \geq \mu\sigma_n$, sliding instability occurs along the fault plane. After analyzing
86 a large number of test data on rock friction and sliding, it is concluded that when the normal
87 stress (σ_n) is less than 100 MPa, the internal friction coefficient (μ) of most crustal rocks is
88 between 0.6 and 1.0 ([Byerlee, 1978](#)). The results of KTB drilling on the continental crust in the
89 German deep hole drilling site show that Byerlee's law applies from the surface to a depth of
90 9.1 km, and the permeable fracture rocks in the range of 3–7 km are very close to Coulomb
91 fracture line when μ is about 0.6. A large number of rock friction mechanical tests in the Three
92 Gorges dam area show that ([Lavrov, 2003](#)), Byerlee's law is also applicable to granite,
93 limestone, sandstone and other rocks in the dam area. The rock friction strength is between $\tau =$
94 $1.10\sigma_n$ and $\tau = 0.65\sigma_n$, with an average value of $\tau = 0.85\sigma_n$. According to Byerlee's law, the
95 angle between the maximum principal stress of Anderson fault and fault plane is 23° – 30° ,
96 which is Byerlee-Anderson theory. μ can quantitatively reflect the friction strength of around
97 fault. When $\mu > 0.6$, the strength of around fault is higher; when $\mu > 0.6$, that is medium; when
98 $\mu < 0.3$, that is weak. Also, the direction of σ_H and σ_h can be roughly inferred according to rock
99 vein, large anticline and syncline.

100 Shendong mining area is located in the north Ordos Basin. It is the largest mining area of
101 coal mine in China. With the increase of mining depth, nonlinear dynamic phenomena occur
102 successively, such as floor heave, spalling, large area roof weighting, gas emission, and so on,
103 which are closely related to in-situ stress. In this paper, based on drilling cores, the KE for
104 testing in-situ stress was carried out. The distribution law of in-situ stress has been analysed,
105 and the stress accumulation level has been evaluated. It has theoretical guiding significance
106 and engineering application value for the mining of Burtai and Baode mines.

107 **2. Geological setting of the study area**

108 Burtai mine is located in the south of Dongsheng country, Ordos City. Its geotectonic
109 division belongs to the mid-eastern of Yimeng uplift and the northeast of Yishan slope in Ordos
110 syncline, North China platform. It is known from the regional structure outline map ([Zhang et](#)
111 [al., 2009; Zhao et al., 2019; Zhao et al., 2018; Ye et al., 2006; He, 2013](#)), Burtai mine is located
112 in the northeast of Wuhai-Ejin Horo banner-Jungar banner deep crust fracture (F11) with a

length of 450 km in EW—NEE. The fractures around it are relatively developed, such as Ordos-Dongsheng crust fracture (F10) with a length of 200 km in NEE, and East Dongsheng basement fracture (F20) with a length of 50km in NW. The complex, broken, uneven and intersecting basement faults lead to the structure of a prism and lattice pattern, which controls the development of fault structures in the upper overburden ([Fig. 1](#) (b)), and constitutes a migration channel for the rise of reducing fluid in deep. It has an important influence on the oil, gas, water and sandstone type uranium deposits in a deep basin. In coal mining, fracture structure is closely related to mine design, production management, disaster prevention and control and mining damage.

[Fig. 1](#). Regional tectonic outline of Burtai mine and Baode mine. (a), location of northern Ordos Basin ([He, 2013](#)); (b), tectonic distribution of northern Ordos Basin. Notes: F1, Ural mountain; F2, Hetao basin; F3, Daqing mountain; F4, Northern margin of Ordos Basin; F5, Horinger; F6, Hanggin banner-Ejin Horo banner; F7, Wuhai North; F8, Dalad banner; F9, Hanggin banner-Togtoh; F10, Ordos-Dongsheng; F11, Wuhai-Ejin Horo banner-Jungar banner; F12, Uxin banner-Shenmu-Fugu; F13, Linfen-Lishi-Pianguan; F14, Leap Hetao basin; F15, Leap Ural mountain ; F16, Leap Ural mountain and Daqing mountain; F17, Leap Daqing mountain; F18, South Linhe; F19, Boundary between northern margin of Ordos Basin fault and Lingle fault; F20, East Dongsheng; F21, Leap near NE fault.

The structural form in Burtai mine is a complex syncline, which is composed of a series of asymmetric secondary gentle open short-axis folds with a dip of 42°–70° in NNW. Within the envelope, the Yan'an formation strikes N10°W–N50°W. The well field structure is generally a nearly horizontal monoclinic structure ([Fig. 1](#) (b)), with the stratum strike of N20°W, the trend of S70°W, the dip of less than 5° and inclined in SW. During field exploration, no large fault, collapse column structure and magmatic rock intrusion were found. Except for a reverse fault with a drop of 0.54m, the rest are medium and small normal faults with a drop of less than 12m, and the strike is NW.

In the process of coal mining, it is found that small and medium-sized folds and faults are widely developed, which have a great impact on coal mining. It is considered that ([Jia, 2008](#); [Qing, 2011](#)), the coal-bearing strata of Yan'an formation are in unconformity contact with its lower Yanchang formation, its upper Zhiluo formation or Yijinhuoluo formation. In the late

143 Middle Jurassic, under the N24–45°E-direction compression, Yimeng uplift took place, and
144 the shallow structural level longitudinal bending fold deformation took place in the Jurassic,
145 forming the capping-sliding type compound syncline structural style. Conjugate shear joints
146 with NNE direction are developed on the outer side of the secondary fold envelope. In the
147 Cretaceous, under the action of N46–65°E nearly horizontal extension, shear and fault rise and
148 fall lead to the occurrence of extensional detachment deformation in a large range, thus forming
149 the widespread development of strata slip faults in Yan'an formation, with accompanied by a
150 large number of high angle normal faults and traction folds. Folds and faults directly affect the
151 distribution of the local stress field.

152 Baode mine is located in Baode County, Shanxi Province. Its geotectonic division belongs
153 to the northeast in Ordos coal accumulating basin, the north section of West Shanxi fold belt,
154 the west of Shanxi Fault uplift, the west of Lvliang structure, and the east of Yellow River
155 graben. The fractures around it are relatively developed, such as Linfen-Lishi-Pianguan crust
156 fracture (F13) in NS, Uxin banner-Shenmu-Fugu crust fracture in NE (F12), and F21 in NW.
157 The strike of faults in the region is dominated by near NS, followed by near WE. The regional
158 tectonic stress field is mainly affected by the Yanshan and Himalayan movement ([Yang et al.,](#)
159 [2014](#)). In the Yanshan period, the compressional stress is dominant, the extensional stress is
160 secondary, and NW-SE compressive stress and NEE-SWW tensile stress are developed. In
161 Himalayan period, the compressional stress changes to NE-SW, the azimuth of σ_1 is N150°E,
162 the dip is 3°, the azimuth of σ_3 is N31°E, and the dip is close to 0°, which leads to a large
163 number of tension joints and weakened compression joints. In the Yanshan period, the fold of
164 axial nearly EW deflected to the axial NW. The superposition of two-periods of tectonic
165 movement causes the direction of σ_1 to change from NW-SE to NE-SE.

166 The Baode mine field is dominated by slightly inclined monoclinic strata. The coal seam
167 is nearly NS trending and inclined to the west, with a dip of 3°–10°. Fold and fault are relatively
168 weak, but joints are very developed. The overall axial direction of the fold is nearly EW. The
169 normal faults account for the majority, and their strike is NE, NW and nearly NS. The joints
170 are significantly affected by lithology, that of Ordovician limestone are relatively developed,
171 and that of coal seam is quite different. The shear joints account for the majority, and the X
172 and goose-type shear joints are developed, which are filled by calcite vein. The landform of

173 Baode mine is characterised by distinct undulating hills. Under the long-term water erosion,
174 the thickly covered surface loess becomes thousands of gullies. The special topography will
175 affect the stress distribution in the mine field.

176 **3. The methods of KE on borehole core for testing in-situ stress**

177 **3.1 Sample preparation and test methods**

178 For the directional rock block with undisturbed shallow bedrock surface or chamber,
179 generally, six or nine small samples ([Qin et al. 1993](#)) are drilled in different directions on the
180 parent rock block, and the samples are cylindrical or square, with a width to height ratio of 1:2.
181 However, the core of ground drilling is different from that of the shallow layer, most of the
182 drilling holes are straight holes, and it is difficult to achieve core orientation. The diameter of
183 the parent rock core is mostly about 75 mm, so it is impossible to drill as required, so it is
184 necessary to reduce drilling number of small samples. KE for testing in-situ stress based on the
185 non-directional core assumes that the vertical stress is one of the principal stresses and the other
186 two are horizontal stresses, it is necessary to process four small cylindrical samples, one along
187 the core axis, three along the perpendicular to the core axis, and drill in 0°, 45° and 90° or 0°,
188 60° and 120° anticlockwise. The diameter and height are 25 and 50mm, which conforms to the
189 rock mechanics test standard. The on-site coring location and sample processing process are
190 shown in [Fig. 2](#), and a total of six drilling holes (Red; Burtai, five; Baode, one) were selected
191 for AE testing. Generally, the influence of core sampling damage on KE can be ignored ([Lavrov,](#)
192 [2003](#)).

193 [Fig. 2](#). Coring and processing of the samples. (a), sampling location in Burtai mine; (b),
194 sampling location in Baode mine; (c), on-site coring (BK220); (d), sampling from rock core;
195 (e), processed samples. Notes: red, the core sampling location tested by AE; light green, the
196 on-site test location by OC.

197 Before the test, 2–4 sensors are used to collect data for small samples, which are placed
198 in the middle of the sample side, as far as possible away from the upper and lower end faces.
199 To ensure the coupling effect between sensor and end face, vaseline or butter is used as the
200 coupling agent, and the sensors are fixed with adhesive tape or plasticine. According to

201 previous research experience ([Qin et al., 1993](#)), in this paper, AE monitoring system is set up
202 with preamplifier gain of 40dB, valve value of 45dB and sampling rate of 1MHz.

203 When the load rate is 0.05–0.25 kN/s or the displacement rate is 0.05–0.6 mm/min in
204 uniaxial loading, the AE effect is better. With the increase of the sample moisture content will
205 lead to the decrease of AE count and energy, so the natural or dry sample should be used ([Yang](#)
206 [et al., 2018](#)). When triaxial loading test is adopted, the stratum stress where the sample is
207 located can be estimated in advance, to set the confining pressure and load the axial load at a
208 constant rate. When the rock is buried shallowly and confining pressure is low, the KE can be
209 used to testing in-situ stress directly by uniaxial loading.

210 For identification of KE points, most scholars choose AE count or count accumulation as
211 parameters, but the author finds that the comprehensive identification method, which is mainly
212 AE count or count accumulation, supplemented by AE energy rate or count rate increment (RI),
213 is easier to determine the KE point. To avoid the interference of friction AE at the initial stage
214 of loading, KE points are usually identified using uniaxial double-cycle loading. Since more
215 AE are produced by crack closure at the beginning of loading, generally, the surge point of the
216 first cycle AE should not be selected, but that of the second loading cycle AE should be used
217 as KE point ([Fig. 3](#)). Moreover, the first cyclic peak load σ_P is less than σ_{Hmax} , σ_P is about 30%
218 of σ_c . Specific identification method of this paper: first, based on AE count or count cumulative
219 versus time, find the counting group, then identify the surge point according to AE energy rate
220 or RI versus time, mutual verification, and comprehensively determine KE point. If there are
221 multiple KE points under cyclic loading or they are not obvious, AE-DRA method can be used
222 to try. The loading mode is multiple cyclic loading controlled by load and displacement. The
223 first cycle σ_P is less than σ_{Hmax} , and the next cycle σ_P is greater than σ_{Hmax} and less than σ_e . It is
224 suggested that the reasonable σ_P in the first cycle is less than 27% of σ_c in siltstone, fine
225 sandstone and coarse sandstone, 40% of σ_c in sandy mudstone, 17% of σ_c in medium sandstone,
226 13% of σ_c in mudstone and limestone, and it does not exceed 63%–70% of σ_c in nest cycles
227 ([Yang et al., 2018](#)). If further KE point recognition is still not ideal, the method of calculating
228 the fractal dimension by G-P algorithm can be used to try. In this paper, three methods are used.
229 [Fig. 3](#). KE point recognition by AE during gradual increase cyclic loading. Notes: σ_{Fi} , the KE
230 point stress corresponding to σ_p in the i cycle; σ_{Ki} , the KE point stress corresponding to σ_{Hmax}

231 in the i cycle.

232 **3.2 Processing of test data**

233 There are different opinions on the determination of principal stress direction of non-
234 directional drilling core ([Li and Dong, 2009](#); [Fa et al., 2017](#)). This section attempts to clarify
235 the magnitude and direction of the principal stress and establish the corresponding calculation
236 equation. For the plane stress state, the stress components σ_x , σ_y and τ_{xy} , $\tau_{xy} = -\tau_{yx}$, on the
237 element body are known, and the normal stress (σ_α) and shear stress (τ_α) on any inclined section
238 (α slope) can be obtained by analytical method:

$$\left. \begin{aligned} \sigma_\alpha &= \sigma_x \cos^2 \alpha + \sigma_y \sin^2 \alpha - 2\tau_{xy} \sin \alpha \cos \alpha \\ &= \frac{\sigma_x + \sigma_y}{2} + \frac{\sigma_x - \sigma_y}{2} \cos 2\alpha - \tau_{xy} \sin 2\alpha \\ \tau_\alpha &= (\sigma_x - \sigma_y) \sin \alpha \cos \alpha + \tau_{xy} (\cos^2 \alpha - \sin^2 \alpha) \\ &= \frac{\sigma_x - \sigma_y}{2} \sin 2\alpha + \tau_{xy} \cos 2\alpha \end{aligned} \right\} \quad (1)$$

240 If the corresponding Mohr stress circle is established, σ_α and τ_α on α slope can also be
241 obtained from it. Then, two principal stress values can be determined as follows:

$$\left. \begin{aligned} \sigma_1 &= \frac{\sigma_x + \sigma_y}{2} + \left[\left(\frac{\sigma_x - \sigma_y}{2} \right)^2 + \tau_{xy}^2 \right]^{\frac{1}{2}} \\ \sigma_2 &= \frac{\sigma_x + \sigma_y}{2} - \left[\left(\frac{\sigma_x - \sigma_y}{2} \right)^2 + \tau_{xy}^2 \right]^{\frac{1}{2}} \end{aligned} \right\} \quad (2)$$

243 If the angle between x -axis and direction of σ_H on the unit is β , and clockwise direction is
244 negative, then:

$$\tan 2\beta = \frac{-2\tau_{xy}}{\sigma_x - \sigma_y} \quad (3)$$

246 To determine the angle between two principal stresses and x -axis, first, calculate β and $\beta \pm 90^\circ$ from Eq. (3), and then compare the magnitude of σ_x and σ_y . If $\sigma_x > \sigma_y$, the angle between
247 the maximum principal stress (σ_1) and x -axis is β ; if $\sigma_x < \sigma_y$, the angle between σ_1 and the x -axis
248 is $\beta \pm 90^\circ$; if $\sigma_x = \sigma_y$, then $\beta = -45^\circ$. That is to say, σ_1 is always inclined to the larger of σ_x and
249

250 σ_y , while σ_2 is inclined to the smaller of them. At the same time, it can be known that the angle
 251 between x -axis and the direction of σ_H is within $\pm 90^\circ$. So, β calculated from Eq. (3) is the angle
 252 between x -axis and direction of σ_H ([Li and Dong, 2009](#); [Fa et al., 2017](#)); in fact there is a certain
 253 deviation.

254 From Eqs. (1) to (3), the magnitude and relative directions of two horizontal principal
 255 stresses can be calculated using the least-squares method. If it is not possible to obtain the KE
 256 point stress of the axial sample along with the core, σ_v can be calculated by the logging density
 257 through the following equation.

$$\left. \begin{aligned} \sigma_H &= \frac{\sigma_{0^\circ} + \sigma_{90^\circ}}{2} + \left| \frac{\sigma_{0^\circ} - \sigma_{90^\circ}}{2} \right| \left[1 + \tan^2 2\beta \right]^{\frac{1}{2}} \\ \sigma_h &= \frac{\sigma_{0^\circ} + \sigma_{90^\circ}}{2} - \left| \frac{\sigma_{0^\circ} - \sigma_{90^\circ}}{2} \right| \left[1 + \tan^2 2\beta \right]^{\frac{1}{2}} \\ \tan 2\beta &= \frac{2\sigma_{45^\circ} - \sigma_{0^\circ} - \sigma_{90^\circ}}{\sigma_{0^\circ} - \sigma_{90^\circ}} \\ \sigma_v &= \int_0^H \rho(h) g dh \end{aligned} \right\} \quad (4)$$

259 With an increase of depth, the mechanical properties of the rock are different from those
 260 of shallow, and the stress is more significantly affected by pore fluid, which can be
 261 characterised by pore pressure. The KE can only measure the relative constant deformation
 262 stress of the memory rock, that is, the effective stress. The real in-situ stress value should be
 263 the effective stress plus the pore pressure, so the expressions of σ_H , σ_h and σ_v considering the
 264 pore pressure are as follows:

$$\left. \begin{aligned} \sigma_H &= \frac{\sigma_{0^\circ} + \sigma_{90^\circ}}{2} + \left| \frac{\sigma_{0^\circ} - \sigma_{90^\circ}}{2} \right| \left[1 + \tan^2 2\beta \right]^{\frac{1}{2}} + \alpha P \\ \sigma_h &= \frac{\sigma_{0^\circ} + \sigma_{90^\circ}}{2} - \left| \frac{\sigma_{0^\circ} - \sigma_{90^\circ}}{2} \right| \left[1 + \tan^2 2\beta \right]^{\frac{1}{2}} + \alpha P \\ \sigma_v &= \int_0^H \rho(h) g dh + \alpha P \end{aligned} \right\} \quad (5)$$

266 3.3 Core orientation using Paleomagnetic technology

267 For non-directional drilling core, the angle between σ_H and 0° mark line can be obtained
 268 from above, while the azimuth of σ_H relative to the geographic north pole requires

269 paleomagnetic orientation technology. The sample is processed into a cylinder with a diameter
270 and height of 25 and 20 mm along the core axis, each testing point processes more than five to
271 seven samples. Draw a straight line along the side parallel generatrix (0° mark line of KE
272 sample) with the top of the core facing upwards, and establish the relative coordinate system
273 rotating around the central axis of the sample, that is, a right-hand coordinate system (Fig. 4).
274 Where, X -axis is the extension direction of sample cross-section dot O toward 0° mark line; Y -
275 axis is 90° clockwise rotation of X -axis; Z -axis is the vertical downward direction of sample
276 axis; OH is the magnetic north direction, the angle between it and X -axis is the magnetic
277 declination (D), which determines the azimuth of the geographical north pole, D is positive
278 along clockwise and negative along counterclockwise; I between OJ vector direction and the
279 horizontal plane is the magnetic dip, I is positive in the northern hemisphere and negative in
280 the southern hemisphere.

281 [Fig. 4.](#) Schematic diagram of relative coordinate system on geomagnetic sample

282 In the paleomagnetic test, 2G superconducting magnetometer in the USA and MMDT80
283 thermal demagnetization meter in the UK are used by thermal demagnetization method. First,
284 the natural remanence (NRM) in samples are measured, and then the samples are demagnetised
285 and cleaned every 50°C . The magnetic declination D_a , magnetic inclination I_a and
286 magnetization of viscous remanence (VRM) in samples are measured. Then, D and I of VRM
287 in the relative coordinate system are obtained by using the principal vector analysis method.
288 Secondly, the average D_a and the average I_a of VRM at each testing point are counted, and the
289 magnetic declination (D_0) of the sampling location relative to the geographic north pole is
290 queried (Burtai, -4.65° ; Baode, -4.18°), then the azimuth of the sample marker line relative to
291 the geographical north pole is $D_0 - D_a$. Finally, according to the angle β (β_0 or $\beta_0 + 90^\circ$) between
292 the 0° mark line and σ_H , the azimuth (α_N) of σ_H relative to the geographic north pole is calculated
293 as:

294
$$\alpha_N = D_0 - D_a - \beta \quad (6)$$

295 **4. Measurement and analysis of in situ stress**

296 **4.1 Distribution characteristics of in-situ stress in Burtai mine**

297 Five boreholes of Burtai mine were selected for in-situ stress testing. They are BK212,
298 BK209, BK213, BK207 and BK220. Their depths are 490–610m with an average of 546m. A
299 group of cores were collected at intervals of about 100m from each borehole, and samples were
300 screened and processed according to the requirements of section 3.1, and KE test was carried
301 out. 343 cores were processed, 338 cores KE stress were obtained. The KE has 263 obvious,
302 accounting for 77.8% of the total, 60 less obvious, accounting for 17.8%, and 15 very
303 insignificant, and accounting for only 4.4%. In the end, a total of 89 groups of in-situ stress
304 data were obtained from five boreholes, among which 35 groups failed to obtain the small core
305 along the core axis, so σ_v could not be tested. Therefore, linear fitting was carried out according
306 to 54 groups of measured σ_v , and then σ_v at depths of measuring points were calculated by the
307 fitting equation.

308 **4.1.1. In-situ stress variation with depth in Burtai mine**

309 [Fig. 5](#) (a-f) show the distribution of σ_H , σ_h , σ_v , k , and azimuth of σ_H at measuring points.
310 The characteristics of the present stress field of five boreholes and nearby areas in Burtai mine
311 are as follows:

312 (1) In the range of 610m depth, σ_H is 1.52–21.04 MPa, σ_h is 1.07–15.76 MPa, σ_v is 2.01–
313 20.55 MPa, which is a general stress level compared with the statistical results of in-situ stress
314 testing in mainland China ([Kang et al., 2010](#)). The three principal stress values have certain
315 discreteness but increase with the increase of depth ([Fig. 5](#) (a-f)). The fitting equations are as
316 follows:

$$\left. \begin{array}{l} \sigma_H = 2.0386 + 0.0241 \times H \\ \sigma_h = 1.2091 + 0.0172 \times H \\ \sigma_v = -0.5257 + 0.0273 \times H \end{array} \right\} \quad (7)$$

318 Among them, the data of BK209 is too discrete, the fitting coefficient is low, and others
319 are more than 0.7. The large discreteness of data is mainly caused by the heterogeneity of rocks
320 caused by different lithology, structure, bedding, and so on. It can be seen from Eq. (7) that σ_v

increases most rapidly with the increase of depth. In shallow mine, the horizontal stress is large. In deep mine, σ_v tends to be close to σ_H .

(2) According to the experience judgment standard ([Wang, 2014](#)), there are 39 with $\sigma_h < 10$ MPa, accounting for 44% of the total; 42 with $\sigma_h < 18$ MPa, accounting for 47%; 8 with $\sigma_H > 18$ MPa, accounting for 9% ([Table 1](#)). Among them, there are 34 groups above 350m, 29 groups with $\sigma_h < 10$ MPa, accounting for 85%; 55 groups below 350m, 11 groups with $\sigma_h < 10$ MPa, accounting for 20%, and 66% with $10 < \sigma_h < 18$ MPa. Therefore, the in situ stress field in Burtai mine is low above 350m and medium below 350m.

[Table 1](#) Distribution of in-situ in different mines

(3) There are main stress regimes: $\sigma_H > \sigma_h > \sigma_v$ (<172 m, I) and $\sigma_H > \sigma_v > \sigma_h$ (170–800 m, II). There are 15 with I, accounting for 17% of the total; 46 with II, accounting for 52%. The former appears as a reverse fault stress mechanism, and the latter appears as a strike-slip fault stress mechanism. The $\sigma_v > \sigma_H > \sigma_h$ stress regime is mainly distributed below 800m, according to Eq. ([7](#)), and it is deeper than that (600 m) of the same stress regime in underground coal mines in China ([Kang et al., 2010](#)), which is consistent with the southern Qinshui Basin (825 m) and western Guizhou province (750 m) ([Chen et al., 2017](#)). The stress state is in good agreement with a large number of extensional structures such as slip faults developed in Yan'an formation in Burtai mine field.

(4) The ratio of σ_H to σ_v is 0.19–2.33, with an average of 1.20 and a mean square deviation of 0.37; the ratio of σ_h to σ_v is 0.14–1.97, with an average of 0.83 and a mean square deviation of 0.31; k is 0.16–2.06, with an average of 1.02 and a mean square deviation of 0.32. Among 89 groups of principal stress data, there are 61 in $\sigma_H > \sigma_v$, accounting for 68.5% of the total. Generally, horizontal stress plays a leading role. The results are in accordance with the transverse isotropic crustal stress model, and it can be expressed as follows:

$$\sigma_H = \frac{1-\nu}{\nu_{xz}} \cdot \sigma_v \quad (8)$$

When $\nu = 0.25$, $\nu_{xz} = 0.5$, $\sigma_H = 1.5 \sigma_v$, the smaller ν_{xz} is, the larger k is, This model can better reflect the in-situ stress characteristics of sedimentary rock strata.

(5) The variation of k with depth is shown in Eq. ([9](#)). Compared with k envelope (Eq. ([10](#))) obtained by Brown and Hoek in the world ([Jia, 2008](#)). In general, the progressive value is

350 different, but they are basically the same in the progressive value of the inner envelope. It can
 351 be seen from [Fig. 6](#) (a) that there are 41 data of $k > 1$, accounting for 46.1%. Above 350m, the
 352 k range is wider. With the increase of depth, the k range becomes narrower. At 350m, $k = 0.98$,
 353 close to 1. The rock mass is in a deep critical state.

354

$$\left. \begin{aligned} k &= \frac{126}{H} + 0.625 \\ \frac{35}{H} + 0.285 &< k < \frac{350}{H} + 0.6 \end{aligned} \right\} \quad (9)$$

355

$$\left. \begin{aligned} k &= \frac{800}{H} + 0.4 \\ \frac{100}{H} + 0.3 &< k < \frac{1500}{H} + 0.5 \end{aligned} \right\} \quad (10)$$

356 (6) The ratio of σ_H to σ_h is 1.07–2.96, with an average of 1.53 and a mean square deviation
 357 of 0.44. The difference between σ_H and σ_h is generally large. Meanwhile, the maximum shear
 358 stress ($(\sigma_1 - \sigma_3) / 2$) is 0.31–6.89 MPa, with an average of 2.05 MPa and a mean square deviation
 359 of 1.18 MPa. It leads to a mixed extension of rock-shear type, which provides conditions for
 360 the development of joint and fault, which is also one of the mechanical reasons for the
 361 development of small and medium-sized faults in the Yan'an Formation. According to statistics
 362 from [Jia \(2008\)](#), the Yan'an formation in Burtai mine has developed small and medium-sized
 363 high angle normal faults, which are composed of small graben, horst, stepped fault and stepped
 364 fault. They are the direct evidence of large shear stress in the rock mass.

365 (7) The in-situ stresses at the same depth are different with different lithology, for example,
 366 the sand mudstone σ_H of 11–13 groups in BK209 is 2.18 times that of the medium sandstone
 367 of 21 and 22 groups in BK212; the sand mudstone σ_H of the 61–63 groups in BK209 is 1.42
 368 times that of the siltstone of 41–43 groups in BK209; the sand mudstone σ_H of 51–53 groups
 369 in BK220 is 1.36 times that of the fine sandstone of 41–43 groups in BK207, and so on. The
 370 most important reason is that σ_c of sandy mudstone is generally high, 30–60 MPa, some of
 371 which are over 80 MPa, and the bearing stress is large, while σ_c of sandstone is low, mostly
 372 less than 30 MPa, with high porosity and weak cementation, so the bearing stress is small.

373 [Fig. 5](#). The relationship between σ_H , σ_h and σ_v vs. depth. (a), BK212; (b), BK209; (c), BK213;
 374 (d), BK207; (e), BK220; (f), σ_H , σ_h and σ_v vs. depth in Burtai mine; (g), σ_H , σ_h and σ_v vs. depth

375 in Baode mine.

376 [Fig. 6](#). Scatter plot of k vs. depth and its relationship. (a), k vs. depth in Burtai mine; (b), k vs.

377 depth in Baode mine.

378 **4.1.2. In-situ stress direction in Burtai mine**

379 Sixteen parent rock core from 100 to 603m depths in Burtai mine are selected for
380 paleomagnetic orientation. The strata are respectively Yijinhuoluo formation, Zhiluo formation
381 and Yan'an formation. The lithology is mainly siltstone, fine sandstone, medium sandstone,
382 coarse sandstone, and so on. One of the measuring points fails to obtain the principal stress
383 direction by KE, so it is impossible to determine the azimuth relative to coordinate North of
384 that. [Fig. 7](#) shows stereoscopic projection and the orthogonal projection of the magnetization
385 directions of some samples. [Table 2](#) shows the test results of the samples. [Fig. 8](#) (a) shows the
386 σ_H azimuth half-rose of samples.

387 [Table 2](#) Paleomagnetic test results of core samples

388 The change of remanent magnetization direction after demagnetization and magnetization
389 intensity and direction of samples can be seen in [Fig. 7](#). The changing trend of magnetization
390 vector of the same group of samples is basically the same, and the difference of different
391 lithologic samples is large. D131 and D132 of coarse sandstones in BK207 thermal
392 demagnetization are from 50° to 500° . After each step, the magnetic declination and dip of
393 VRM are both relatively stable. However, but the magnetization vector of D511 and D512 of
394 medium sandstones turns, and the intensity is weakened after demagnetization at 500° , so this
395 point should be abandoned. The principles to be followed in the selection of thermal
396 demagnetization points are α_{95} confidence ErAng \pm error < 16 ; more than three selected points;
397 temperature above 100° - 200° , and so on.

398 [Fig. 7](#). Thermal demagnetization curves of samples in BK207. (a), D131; (b), D132; (c), D511;
399 (d), D512.

400 Among the 63 measuring points in [Fig. 8](#) (a), there is 22 σ_H orientation between $N30^\circ E$
401 and $N75^\circ E$, accounting for 34.92% of the total, and 14 between $N30^\circ E$ and $N75^\circ E$, accounting
402 for 22.22%. Therefore, the dominant orientation of σ_H in Burtai mine is NE-NNE, followed by

403 NW.

404 [Fig. 8](#). Half rose diagram of σ_H azimuth. (a), σ_H azimuth in
405 Baode mine.

406 Study of focal mechanism solution, HF and hole wall collapse in Ordos area show that the
407 orientation of σ_H is NE-NEE. That obtained by paleomagnetic combined with KE is consistent
408 with the above results, and some measuring points are quite different, which is mainly related
409 to the local geological structure, rock mass structure and test process error. Through a large
410 number of mine geological structure observation and surface geological survey ([Jia, 2008](#)), it
411 is believed that the fault strike of the mine field is mainly NNE, followed by NW, and the basic
412 pattern of the extensional structure is the capping-sliding type. So the orientation of σ_H is
413 parallel to the fault trend. When the angle between the orientation of σ_H and the axial direction
414 of the roadway is 0° – 30° , which is conducive to the stability of it.

415 **4.2 Distribution characteristics of in-situ stress in Baode mine**

416 The borehole beside Baode power plant was selected for the in-situ stress test. The depth
417 of borehole is 416m. A group of cores were collected every 50m. 85 cores were processed, 85
418 cores KE stress were obtained. The KE has 44 obvious, accounting for 51.8% of the total, 19
419 less obvious, accounting for 22.4%, and 22 very insignificant, and accounting for only 25.8%.
420 In the end, a total of 24 groups of in-situ stress data were obtained, including 13 groups of
421 measured σ_v and 11 groups of calculated σ_v by the fitting equation.

422 **4.2.1. In-situ stress variation with depth in Baode mine**

423 [Fig. 5](#) (g) shows the distribution of σ_H , σ_h , σ_v , k , and the azimuth of σ_H at measuring points.
424 The characteristics of the present stress field of the power plant and nearby areas in Baode mine
425 are as follows:

426 (1) In the range of 420m depth, σ_H is 3.99–15.15 MPa, σ_h is 0.71–9.63 MPa, σ_v is 1.26–
427 10.01 MPa. The three main stress values are all discrete but increase with the increase of depth
428 ([Fig. 5](#) (g)). The fitting equations are as follows:

429

$$\left. \begin{array}{l} \sigma_H = 3.5656 + 0.0161 \times H \\ \sigma_h = 0.7081 + 0.0189 \times H \\ \sigma_v = -0.5935 + 0.0267 \times H \end{array} \right\} \quad (11)$$

430 (2) There are 23 with $\sigma_h < 10$ MPa, accounting for 96% of the total, and only one with 10
 431 $< \sigma_h < 18$ MPa ([Table 1](#)). Therefore, the in situ stress in Baode mine belongs to the low in situ
 432 stress field as a whole.

433 (3) There are main stress regimes: $\sigma_H > \sigma_h > \sigma_v$ (<170m, I) and $\sigma_H > \sigma_v > \sigma_h$ (170–400 m,
 434 II). There are 10 with I or II, accounting for 42% of the total respectively. The $\sigma_v > \sigma_H > \sigma_h$
 435 stress regime is mainly distributed at a depth below 400m, according to Eq. (11), and it is
 436 shallower than that (600–750 m) of the same stress regime in underground coal mines in China
 437 ([Kang et al., 2010](#); [Chen et al., 2017](#)).

438 (4) The ratio of σ_H to σ_v is 0.72–3.61, with an average of 1.76 and a mean square deviation
 439 of 0.81; the ratio of σ_h to σ_v is 0.31–1.68, with an average of 0.96 and a mean square deviation
 440 of 0.34; k is 0.66–2.44, with an average of 1.36 and a mean square deviation of 0.50. Among
 441 24 groups of the principal stress data, there are 20 in $\sigma_H > \sigma_v$, accounting for 83.3% of the total.

442 (5) The variation of k with depth is shown in Eq. (12). It is similar to the envelope line of
 443 k obtained by Brown and Hoek in the world, but there are some differences in the progressive
 444 value, which is close to that of 0.3 and 0.5 of the inner and outer envelope lines. According to
 445 [Fig. 6](#)(b), there are 18 data of $k > 1$, accounting for 75%. Above 350m, the k range is wider.
 446 With the increase of depth, the k range becomes narrower. At 350m, $k = 1.02$, close to 1. Much
 447 like the Burtai Mine, the rock mass is in a deep critical state.

448

$$\left. \begin{array}{l} k = \frac{72}{H} + 0.817 \\ \frac{70}{H} + 0.32 < k < \frac{210}{H} + 0.46 \end{array} \right\} \quad (12)$$

449 (6) The ratio of σ_H to σ_h is 1.07–7.38, with an average of 2.04 and a mean square deviation
 450 of 1.42. The difference between σ_H and σ_h is generally large. Meanwhile, $(\sigma_1 - \sigma_3) / 2$ is 0.24–
 451 4.44 MPa, with an average of 1.46 MPa and a mean square deviation of 0.86 MPa, which leads
 452 to large shear stress in the rock mass, providing favorable conditions for development of joint
 453 and fault in Baode mine.

454 **4.2.2. In-situ stress direction in Baode mine**

455 Eight parent rock cores from 99.1 to 340.6m in Baode power plant are selected for
456 paleomagnetic orientation. The strata are Shangshihezi formation, Shanxi formation, Taiyuan
457 formation and Fengfeng formation respectively. The lithology is mainly fine sandstone,
458 medium sandstone, sandy mudstone, mudstone and limestone. [Table 2](#) shows the test results
459 of the samples. [Fig. 8](#) (b) shows σ_H azimuth half-rose of samples.

460 Among the 19 measuring points in [Fig. 8](#) (b), there is 14 σ_H orientation between NS and
461 N45°E, accounting for 73.7% of the total. Therefore, the dominant orientation of σ_H in Baode
462 mine is NEE, which is generally consistent with the NNE-NE obtained from the regional focal
463 mechanism solution.

464 **5. Discussion**

465 **5.1 Comparison of in-situ stress test results**

466 **5.1.1. Comparison of in-situ stress test results in Burtai mine**

467 In-situ stress testing of three boreholes ([Fig. 2](#), light green) by OC in the first and second
468 panels of Burtai mine was carried out by Anhui University of science and technology. The
469 depth is 348m. KE stresses of three measuring points close to their depth are selected and
470 compared with that. Their locations are different, but the terrain is flat, so we still try to analyze
471 them.

472 [Table 3](#) Comparison of test results between KE and OC, HF

473

474 According to [Table 3](#), the seven stresses of KE are greater than that of OC, accounting for
475 77.8% of the total. The relative error of σ_H is 6.44%–25.37%, that of σ_h is 10.94%–34.49%,
476 that of σ_v is 12.66%–19.35%, and that of three principal stress is 14.90%, 19.67% and 15.47%
477 respectively. Therefore, the error of test results between KE and OC is small. Considering the
478 different test locations, the error is within the reasonable range of engineering, which can meet
479 the geological evaluation and stability of engineering, and verify the reliability of KE for testing
480 in-situ stress.

481 In-situ stress testing by HF in Yitai mining area and Hongqinghe area of Dongsheng coal
482 field was carried out ([Liu, 2011](#)), and KE stresses of ten measuring points close to their depth
483 are selected and compared with that. The three measuring points were calculated by Eq. (7),
484 and the results are shown in [Table 3](#). The eighteen stresses of KE are greater than that of HF,
485 accounting for 54.5% of the total. The relative error of σ_H is 9.81%–45.24%, that of σ_h is 0–
486 51.73%, that of σ_v is 0.65%–81.80%, and that of three principal stress is 21.40%, 17.64% and
487 23.79%, respectively. Due to the influence of geological structure and depth, the relative error
488 is relatively large above 100m, and the test result is also discrete. However, considering the
489 change of the location of measuring points and the occurrence of the coal seam, the test result
490 error is still within the reasonable range required by the project. Therefore, the test results of
491 the two methods are consistent to a certain extent.

492 Three major tectonic movements of Indochina, Yanshan and Xishan occurred in the
493 Mesozoic and Cenozoic strata in Ordos Basin. At the end of the Jurassic, the basin was subject
494 to horizontal tectonic compression in NWW-SEE and the second tectonic thermal event. It
495 formed σ_H in NWW-SEE and EW and NW-SE conjugate shear fractures in the Jurassic Yan'an
496 Formation ([Gao et al., 2020](#); [Ju et al., 2019](#)). From the late Cretaceous to Paleogene, the basin
497 was subjected to NNE-SSW horizontal tectonic compression and the third tectonic thermal
498 event, resulting in strata denudation thickness of 600–3200m ([Ma et al., 2020](#); [Meng, 2016](#); [Ng
499 et al., 2017](#)). Under tectonic compression and uplift denudation, σ_H in NNE-SSW and NS and
500 NE-SW conjugate shear fractures were formed in the Late Jurassic, Cretaceous and Neogene.
501 Under the thrust or nappe action of peripheral faults into the basin, the basin is uplifted as a
502 whole, and low angle or interlayer sliding occurs, forming slip thrust fault, which releases the
503 energy accumulated by orogeny movements around the basin, and the strata are not deformed
504 obviously ([Li et al., 2014](#); [Wu et al., 2017](#); [Xiao et al., 2020](#)). However, most of the basement
505 faults have been activated, and the deep fractures have obvious control on the shallow ones.

506 During field exploration, 11 large and medium-sized faults are developed in the northern
507 Shenmu mine area of Shengfu coal field, all of which are tensional high angle normal faults with
508 strike NW and dip of 55°–80°. The drop is 10–80m, and the extension is less than 16km. It can
509 be inferred that the σ_I direction is roughly N40°E–N80°E ([Ju et al., 2015](#); [Ju et al., 2020](#); [Li et
510 al., 2019](#)). Based on the research results of focal mechanism solution, HF, hole wall collapse,

511 OC, fault sliding vector and earthquake surface rupture ([Ju et al., 2017](#); [Wang et al., 2018](#);
512 [Deng and Sheng, 2015](#); [Sheng et al., 2015](#)), it is considered that the present σ_1 direction in north
513 Ordos area is NE-NEE. There are six points of ten measuring points σ_1 in N28.3°E–N54.1°E
514 in Yitai mining area, and four are in N18.9°W–N63.6°W, most of which are in NE; the
515 orientations of the three fracture surfaces of the hydraulic fracture holes are N65.0°E, N61.0°E,
516 and N54.0°E in Hongqinghe mining area, generally in NE-NEE. In situ stress test of 42 coal
517 seam in Burtai mine was performed by Taiyuan University of technology. σ_1 is about N30°E,
518 which is vertical to the roadway axis of 42103 working face, and there is large tectonic stress.
519 The results in this paper show that the dominant orientation of σ_H in Burtai mine is NE- NNE,
520 followed by NW, and that of σ_H in Baode mine is NEE (section 5.1.2). It is related to the
521 Triassic and Jurassic tectonic movement in the Ordos Basin. σ_H in NWW-SEE is formed by
522 the Yanshan movement, and σ_H in NNE-SSW is the product of Himalayan movement. The
523 two-periods of tectonic movement since Mesozoic resulted in the deflection of σ_H orientation
524 in Shendong mining area. At the same time, the dominant orientation of σ_H in Burtai mine is
525 also roughly consistent with the main fault strike (near NEE) of surface Huhewusu ditch in
526 south. Therefore, the present σ_H orientation in Shendong mining area obtained by KE combined
527 with paleomagnetic orientation is consistent with the above results, and some measuring points
528 are quite different, which is mainly related to the local geological structure, rock mass structure,
529 topography and landform, and error of the test process.

530 5.1.2. Comparison of in-situ stress test results in Baode mine

531 In-situ stress testing of three boreholes ([Fig. 2](#), light green) by OC in the third panel of
532 Baode mine was carried out by Anhui University of science and technology. The depth is 485m.
533 KE stresses of three measuring points close to their depth are selected and compared with that.
534 Eq. (11) is used to calculate the 2 # and 6 # measuring points. According to [Table 4](#), the seven
535 stresses of KE are greater than that of OC, accounting for 77.8% of the total. The relative error
536 of σ_H is 8.46%–12.41%, that of σ_h is 27.18%–35.65%, that of σ_v is 34.82%–45.59%, and that
537 of principal stress is 9.91%, 30.82% and 39.84% respectively, among which that between
538 fitting equation and OC is the largest.

539 The stress values measured by KE is compared with that measured by ASR ([Xu, 2018](#)),
540 and the cores of the same depth in the same borehole is selected. The samples of 51–53 and
541 62–64 groups in [Table 4](#) are selected by KE, and that of BD-2 (275.5m) and BD-6 (346.0m)
542 are selected by ASR, among which the average values of σ_H , σ_h and σ_v of 51–53 groups are
543 8.28, 6.16 and 7.31 MPa, respectively, and that of σ_H , σ_h and σ_v of BD-2 are 6.8, 4.7 and 7.3
544 MPa, with relative errors of 17.90%, 23.71% and 0.08%; the average values of σ_H , σ_h and σ_v of
545 62–64 groups are 8.34, 6.91 and 9.41 MPa respectively, and that of σ_h , σ_h and σ_v of BD-6 are
546 7.9, 7.3 and 9.4 MPa, with relative errors of 5.22%, 5.68% and 0.13%. The average relative
547 errors of the principal stresses for them are 11.56%, 14.69%, and 0.11%, respectively.

548 [Table 4](#) Comparison of test results between KE and OC, ASR

549 Therefore, the error of e test results of KE method and ASR method is small, and that of
550 KE and OC is larger. Considering the different test locations, and the two groups of data are
551 calculated by Eq. [\(11\)](#). If the two groups are removed, the errors are within the reasonable range
552 of the project, which can meet the requirements of engineering geological evaluation and
553 stability analysis. So, Reliability of KE has been verified.

554 **5.2 Analysis of stress accumulation level of rock**

555 Based on the Byerlee Anderson theory and in-situ stress test results, the stress state of
556 boreholes in two mines is drawn, as shown in [Fig. 9](#). None of the six boreholes has a measured
557 point with $\mu > 0.6$, and σ_H is all on the left of the lower limit of Byerlee range, and $\mu < 0.3$.
558 Below 350m, a small amount of data in Burtai mine is between $0.6 > \mu > 0.3$, which indicates
559 that with the increase of depth, the stress accumulation level is increasing. Therefore, it can be
560 concluded that the friction strength of the faults around the boreholes in two mines is weak, the
561 stress level is low, and they are in a relatively calm period, and the faults and surrounding areas
562 are in a relatively stable state.

563 [Fig. 9](#). The relationship between principal stress vs. μ . (a), principal stress vs. μ in Burtai mine;
564 (b), principal stress vs. μ in Baode mine.

565 The sliding failure caused by the increase of shear stress is a common fracture
566 phenomenon in the earth's crust. The main controlling factors are the maximum shear stress

567 and the normal stress of vertical shear plane. Therefore, the μ_{md} and μ_{mh} calculated based on in-situ stress are also indicators to characterize the regional stress accumulation level ([Jamison and Cook, 1980](#)). The relationship between μ_m and μ is as follows:

$$570 \quad \mu_m = \mu / (1 + \mu^2)^{0.5} \quad (13)$$

571 The expressions of indexes μ_{md} and μ_{mh} are as follows:

$$572 \quad \left. \begin{aligned} \mu_{md} &= \frac{\sigma_1 - \sigma_3}{\sigma_1 + \sigma_3} \\ \mu_{mh} &= \frac{\sigma_1 - \sigma_3}{\sigma_1 + \sigma_3 - 2P_0} \end{aligned} \right\} \quad (14)$$

573 Where σ_1 , σ_3 and P_0 represent the maximum principal stress, the minimum principal stress
 574 and the pore pressure respectively. In the shallow low permeability rocks of the crust, P_0 is
 575 roughly equal to the static pressure of the water column ([Townend and Zoback, 2000](#)). To some
 576 extent, μ_{md} and μ_{mh} only represent the stress accumulation level, independent of the stress
 577 direction. The larger the value is, the greater the shear stress around the fault is, the higher the
 578 stress accumulation level is, the greater the possibility of fault activity is, and vice versa
 579 ([Jamison and Cook, 1980](#)). The shallow μ_m is mostly 0.7, the deep μ_m is 0.5 ([Tuncay and Ulusay, 2008](#)), so when μ_m is 0.5–0.7, the crustal stress accumulation is in its friction limit state; when
 580 μ_m is close to 0.5–0.7, the stress accumulation level is higher; when μ_m is less than 0.3, that is
 581 lower.

583 [Figure 10](#) gives the distribution of μ_{md} and μ_{mh} with depth in two mines. In dry rock, the
 584 μ_{md} in Boertai mine is 0.04–0.76, with an average of 0.24 and a mean square deviation of 0.14,
 585 among which, $\mu_{md} > 0.1$, accounting for 87.6% of the total, and only two points with $\mu_{md} > 0.6$,
 586 and they are 0.76 and 0.75, 66 points with $\mu_{md} < 0.3$, accounting for 74.2% and 85 points with
 587 $\mu_{md} < 0.5$, accounting for 95.5%; the μ_{md} in Baode mine is 0.03–0.76, with an average of 0.32
 588 and a mean square deviation of 0.19, among which, $\mu_{md} > 0.1$, accounting for 87.5%, and only
 589 three points with $\mu_{md} > 0.6$, and they are 0.60, 0.76 and 0.61 respectively, 13 points with $\mu_{md} <$
 590 0.3, accounting for 54.2%, 19 points with $\mu_{md} < 0.5$, accounting for 79.2%; the average values
 591 of μ_{md} are 0.33 (Burtai), 0.42 (Baode) above 170m, and they are both 0.23 below 170m. In
 592 hydrostatic pressure rock, after four outliers are removed in Burtai mine, μ_{mh} is 0.05–0.89, with
 593 an average of 0.32 and a mean square deviation of 0.19, among which, $\mu_{mh} > 0.1$, accounting

594 for 91.8% of the total, only 8 points with $\mu_{mh} > 0.6$, 49 points with $\mu_{mh} < 0.3$, accounting for
595 57.6%, 71 points with $\mu_{mh} < 0.5$, accounting for 83.5%; after two outliers are removed in Baode
596 mine, μ_{mh} is 0.04–0.74, with an average of 0.31, with an average of 0.31 and a mean square
597 deviation of 0.19, among which, $\mu_{mh} > 0.1$, accounting for 86.4%, and only one with $\mu_{mh} > 0.1$,
598 and it is 0.74, 13 points with $\mu_{mh} < 0.3$, accounting for 59.1%, 17 points with $\mu_{mh} < 0.5$,
599 accounting for 77.3%; the average values of μ_{mh} are 0.47 (Burtai), 0.50 (Baode) above 170m,
600 and they are 0.35(Burtai), 0.32 (Baode) below 170m.

601 Fig. 10. Scatter plot of μ_{md} and μ_{mh} vs. depth and its relationship. (a), μ_{md} vs. depth and its
602 relationship in Burtai mine; (b), μ_{md} vs. depth and its relationship in Baode mine; (c), μ_{mh} vs.
603 depth and its relationship in Burtai mine; (d), μ_{mh} vs. depth and its relationship in Baode mine.

604 No matter in dry rocks or hydrostatic pressure rocks, the friction coefficient of faults in
605 the two mines is low, the average values of μ_{md} are 0.23–0.33, 0.23–0.44, μ_{mh} are 0.35–0.47,
606 0.32–0.50, which are less than the lower limit (0.6) of strike-slip faults slip. It shows that the
607 fracture stress state around the study area is lower than the friction limit state, which is at a low
608 level as a whole, and the risk of seismic activity is low. Historically, the number of earthquakes
609 in Ordos City and its vicinity was not many, and the intensity was not high, and the regional
610 in-site stress is in the accumulation stage, which does not exclude the possibility of small and
611 micro earthquakes. From the comparison of mine, the stress accumulation of Baode mine is
612 greater than that of Burtai mine.

613

614 6. Conclusions

615 Based on elastic mechanics and paleomagnetic reorientation technology, the in-situ stress
616 test method based on KE of borehole core is established. This method is used to test and analyze
617 the distribution characteristics of present stress in and around the boreholes of Burtai mine and
618 Baode mine, and the test results are compared with that of OC, ASR and adjacent mine HF.
619 Based on Byerlee-Anderson theory, the stress accumulation level of the rock mass is discussed.
620 The main conclusions are as follows:

621 (1) For the non-directional drilling core, based on the elastic mechanics, the magnitude

622 and direction of the principal stress measured by KE are derived. The angle between the
623 direction of σ_H and the marker line is β_0 or $\beta_0 + 90^\circ$. The azimuth of σ_H relative to the geographic
624 north pole is calculated as $D_0 - D_a - \beta$.

625 (2) The σ_H , σ_h and σ_v in two mines increase with increasing of depths. The ratios of σ_H , σ_h
626 to σ_v are 1.20, 0.83 (Burtai), 1.76 and 0.96 (Baode), respectively. k is 1.02 (Burtai) and 1.36
627 (Baode). Generally, horizontal stresses play a leading role. The ratio of σ_H to σ_h is 1.53 (Burtai)
628 and 2.04 (Baode), and $(\sigma_1 - \sigma_3)/2$ is 2.05 MPa (Burtai) and 1.46 MPa (Baode). There are main
629 stress regimes in NOB: $\sigma_H > \sigma_h > \sigma_v$ (Burtai, <172m; Baode, <170m) and $\sigma_H > \sigma_v > \sigma_h$ (Burtai,
630 170-800 m; Baode, 170-400 m), and the $\sigma_v > \sigma_H > \sigma_h$ stress regime is mainly distributed in
631 moderately deep to deep coal mines. For rock masses with a depth of 350m, $k ((\sigma_H + \sigma_h)/2\sigma_v)$
632 tends to 1, indicating that deep critical state will gradually emerge.

633 (3) The test results were compared with that of OC, ASR and HF. The relative errors of
634 σ_H , σ_h and σ_v are 14.90%, 19.67%, 15.47% (Burtai) and 10.74%, 22.76%, 19.97% (Baode), and
635 they are all within a reasonable range required by the project, which can meet the requirements
636 of the geological evaluation and stability analysis of the engineering rock mass. Therefore, it
637 verifies the reliability of KE method.

638 (4) The dominant orientation of σ_H in Burtai mine is NE- NNE, followed by NW, and that
639 of σ_H in Baode mine is NEE. It is related to the Triassic and Jurassic tectonic movement in the
640 Ordos Basin. σ_H in NWW-SEE is formed by the Yanshan movement, and σ_H in NNE-SSW is
641 the product of Himalayan movement, which is consistent with that (NE-NEE) of earthquake
642 focal mechanisms in this area.

643 (5) Under dry rocks or hydrostatic pressure rocks, the friction coefficient of faults are both
644 low, the average values of μ_{md} are 0.23–0.33 (Burtai), 0.23–0.44 (Baode), μ_{mh} are 0.35–0.47
645 (Burtai), 0.32–0.50 (Baode), which is less than the lower limit of strike-slip faults slip,
646 indicating that the fracture stress with a low level around the study area is lower than the friction
647 limit stress. The stress accumulation level in Baode mine is slightly larger than that in Burtai
648 mine.

649

650 **Acknowledgements**

651 This study was supported by Scientific and Technological Innovation Programs of Higher
652 Education Institutions in Shanxi (2019L0772), the Key Research Development Program of
653 Shanxi Province (201903D121070), Shenhua Shendong Coal Branch Technology Innovation
654 Project (2018156), and Datong Basic Research Project (2018156).The authors especially thank
655 Senior engineer Guijun Song, Erlin Wang and Guoqiang Xie of Shendong Coal Branch for
656 their help in the on-site core collection, and thank Professor Yixin Zhao for his help in writing
657 paper.

658

659 **Declaration of Interest statement**

660 The authors declare that they have no known competing financial interests or personal
661 relationships that could have appeared to influence the work reported in this paper.

662 **References**

- 663 Anderson, E. M., 1942. The dynamics of faulting and dyke formation, with applications to
664 Britain. *Nature*. 62(4), 651–652. <https://doi.org/10.1086/626182>.
- 665 Brown, E.T., Hoek, E., 1978. Trends in relationships between measured in-situ, stresses and
666 depth. *Int. J. Rock. Mech. Min. Sci. Geo.* 15(4), 211–215. [https://doi.org/10.1016/0148-9062\(78\)91227-5](https://doi.org/10.1016/0148-9062(78)91227-5).
- 668 Byerlee, J.D., 1978. Friction of rocks. *Pure. Appl. Geophys.* 116(4/5), 615–626. <https://doi.org/10.1007/bf00876528>.
- 670 Chen, S.D., Tang, D.Z., Tao, S., Xu, H., Li, S., Zhao, J.L., Ren, P.F., Fu, H.J., 2017. In-situ
671 stress measurements and stress distribution characteristics of coal reservoirs in major
672 coalfields in China: Implication for coalbed methane (CBM) development. *Int. J. Coal
673 Geol.* 182, 66–84. <https://dx.doi.org/10.1016/j.coal.2017.09.009>.
- 674 Deng, S.Q., Sheng, S.Z., 2015. The crustal stress field around the Ordos block. *North. Chin.
675 Earthq. Sci.* 33(2), 55–62.
- 676 Fa, L., Xie, B.Z., Xi, B.J., Shen, N., Zhang, S.L., 2017. A method for predicting principal
677 stresses of underground rock. *J. Xi'an Univ. Posts and Telecomm.* 22(3), 87–92.
678 <https://dx.doi.org/10.13682/j.issn.2095-6533.2017.03.016>.
- 679 Gao, Y., Jiang, Z.X., James, L.B., Zhang, J.G., 2020. Soft-sediment deformation structures as
680 indicators of tectono-volcanic activity during evolution of a lacustrine basin: A case study
681 from the Upper Triassic Ordos Basin, China. *Mar. Petrol. Geol.*, 115(5), 104250

- 682 <https://doi.org/10.1016/j.marpetgeo.2020.104250>.
- 683 Ge, W.F., Zhang, F., Chen, M., Jin, Y., Lu, Y.H., Hou, B., 2015. Research on geostress
684 measurement using DRA-Kaiser method in salt-gypsum formation. Chin. J. Rock. Mech.
685 Eng. 34(S1), 3138–3142. <https://doi.org/10.13722/j.cnki.jrme.2014.0132>.
- 686 Goodman, R.E., 1963. Subaudible noise during compression of rocks. Geol. Soc. Am. Bull.
687 74(4), 487–490. [https://dx.doi.org/10.1130/0016-7606\(1963\)74\[487: sndcor\]2.0.co;2](https://dx.doi.org/10.1130/0016-7606(1963)74[487: sndcor]2.0.co;2).
- 688 He, Z.J., 2013. The application of gravity and magnetic data processing and interpretation in
689 regional tectonic analysis of Ordos Basin. Chin. Univ. Geosci. (Beijing), Beijing. pp 30–
690 98.
- 691 Hoek, E., Brown, E.T., 2019. The Hoek – Brown failure criterion and GSI–2018 edition. J.
692 Rock. Mech. Geotech. Eng., 11, 445–463. <https://doi.org/10.1016/j.jrmge.2018.08.001>.
- 693 Holcomb, D.J., 1983. Using Acoustic emissions to determine in-situ stress: problems and
694 promise. 57, 11–21.
- 695 Jamison, D.B., Cook, N.G.W., 1980. Note on measured values for the state of stress in the
696 Earth's crust. J. Geophys. Res. Sol. Ea. 85(B4), 1833–1838. <https://dx.doi.org/10.1029/JB085iB04p01833>.
- 698 Jia, J.W., 2008. Study on the geometry of extensional structure in the Burtai well field. J. Chin.
699 Coal. Soc., 33(11), 1253–1256.
- 700 Ju, J.F., Xu, J.L., Zhu, W.B., 2015. Longwall chock sudden closure incident below coal pillar
701 of adjacent upper mined coal seam under shallow cover in the Shendong coalfield. Int. J.
702 Rock. Mech. Min., 77:192–201. <https://doi.org/10.1016/j.ijrmms.2015.04.004>.
- 703 Ju, W., Jiang, B., Qin, Y., Wu, C.F., Wang, G., Qu, Z.H., Li, M., 2019. The present-day in-situ
704 stress field within coalbed methane reservoirs, Yuwang Block, Laochang Basin, south
705 China. Mar. Petrol. Geol., 102(5), 61–73. <https://doi.org/10.1016/j.marpetgeo.2018.12.030>.
- 706 Ju, W., Niu, X.B., Feng, S.B., You, Y., Xu, K., Wang, G., Xu, H.R., 2020. Present-day in-situ
707 stress field within the Yanchang Formation tight oil reservoir of Ordos Basin, central
708 China. J. Petrol. Sci. Eng., 187(4), 106809. <https://doi.org/10.1016/j.petrol.2019.106809>.
- 709 Ju, W., Shen, J., Qin, Y., Meng, S.Z., Wu, C.F., Shen, Y.L., Yang, Z.B., Li, G.Z., Li, C., 2017.
710 In-situ stress state in the Linxing region, eastern Ordos Basin, China: Implications for
711 unconventional gas exploration and production. Mar. Petrol. Geol., 86(9), 66–78.
712 <https://doi.org/10.1016/j.marpetgeo.2017.05.026>.
- 713 Kanagawa, T., Hayashi, M., Nakasa, H., 1976. Estimation of spatial geo-stress components in
714 rock samples using the Kaiser effect of acoustic emission. Doboku Gakkai Ronbunshu.
715 258, 63–75.
- 716 Kang, H.P., Zhang, X., Si, L., Wu, Y., Gao, F., 2010. In-situ stress measurements and stress
717 distribution characteristics in underground coal mines in China. Eng. Geol. 116, 333–345.
718 <https://doi.org/10.1016/j.enggeo.2010.09.015>.
- 719 Kurita, K., Fujii, N., 1979. Stress memory of crystalline rocks in acoustic emission. Geophys.
720 Res. Lett. 6(1), 9–12. <https://doi.org/10.1029/GL006i001p00009>.
- 721 Lavrov, A., 2003. The Kaiser effect in rocks: principles and stress estimation techniques. 40(2),

- 722 151–171. [https://doi.org/10.1016/s1365-1609\(02\)00138-7](https://doi.org/10.1016/s1365-1609(02)00138-7).
- 723 Li, C., Nordlund, E., 1993. Experimental verification of the Kaiser effect in rocks. Rock. Mech. Rock. Eng. 26(4), 333–351. <https://doi.org/10.1007/BF01027116>.
- 725 Li, G.Q., Yan, D.T., Zhuang, X.G., Zhang, Z., Fu, H.J., 2019. Implications of the pore pressure
726 and in situ stress for the coalbed methane exploration in the southern Junggar Basin, China.
727 Eng. Geol., 262(11), 105305<https://doi.org/10.1016/j.enggeo.2019.105305>.
- 728 Li, Y., Tang, D.Z., Xu, H., Yu, T.X., 2014. In-situ stress distribution and its implication on
729 coalbed methane development in Liulin area, eastern Ordos basin, China. J. Petrol. Sci. Eng.,
730 122(10), 488–496. <https://doi.org/10.1016/j.petrol.2014.08.010>.
- 731 Li, Y.X., Dong, P.C., 2009. In-situ stress measurement of reservoir using Kaiser effect of rock.
732 Chin. J. Rock. Mech. Eng. 28(S1), 2802–2802. <https://doi.org/10.3321/j.issn:1000-6915.2009.z1.033>.
- 734 Lieurance R.S., 1933. Stresses in foundation at Boulder (Hoover) dam. U.S. Bureau of
735 Reclamation Technical Memorandum. 12, 346.
- 736 Liu, J., 2011. In-situ stress measurements and study on distribution characteristics of stress
737 fields in underground coal mines in Yitai mining area. J. Chin. Coal. Soc. 36(4), 562–566.
738 <https://doi.org/10.3724/SP.J.1077.2011.00271>.
- 739 Ma, W.J., Hou, L.H., Luo, X., Liu, J.Z., Tao, S.Z., Guan, P., Cai, Y.W., 2020. Generation and
740 expulsion process of the Chang 7 oil shale in the Ordos Basin based on temperature-based
741 semi-open pyrolysis: Implications for in-situ conversion process. J. Petrol. Sci. Eng.,
742 190(7), 107035. <https://doi.org/10.1016/j.petrol.2020.107035>.
- 743 Meng, Z.P., Shi, X.C., Li, G.Q., 2016. Deformation, failure and permeability of coal-bearing
744 strata during longwall mining. Eng. Geol., 208(5), 69–80. <https://doi.org/10.1016/j.enggeo.2016.04.029>.
- 745 Michihiro, K., Fujiwara, T., Yoshioka, H., 1985. Study on estimating geostresses by the kaiser
746 effect of AE. U.S. Symposium on Rock Mechanics. [https://doi.org/10.1016/0148-9062\(86\)90772-2](https://doi.org/10.1016/0148-9062(86)90772-2).
- 747 Ng, H.M., Ge, L.L., Du, Z.Y., Wang, S.R., Ma, C., 2017. Satellite radar interferometry for
748 monitoring subsidence induced by longwall mining activity using Radarsat-2, Sentinel-1
749 and ALOS-2 data. Int. J. Appl. Earth. Obs., 61(9), 92–103. <https://doi.org/10.1016/j.jag.2017.05.009>.
- 750 Peng, S.S., Li, H.M., Zhou, Y., 2015. Study on strata control in Shendong and Zhungeer mining
751 areas. Science Press, Beijing. pp 20–80.
- 752 Qian, Q.H., 2012. Challenges and countermeasures for safety of underground engineering
753 construction. Chin. J. Rock. Mech. Eng. 31(10), 1945–1956.
- 754 Qin, S.Q., Li, Z.D., Zhang, X.Y., Deng, R.G., 1993. Introduction to rock acoustic emission
755 technology. Southwest Jiaotong University Press, Chengdu, pp 60–130.
- 756 Qing, L.H., 2011. Study on mechanism of overburden rock failure during coal mining with
757 shallow depth and thin bedrock. Procedia. Eng., 26, 228–235.
758 <https://doi.org/10.1016/j.proeng.2011.11.2162>[Get rights and content](#).

- 762 Sheng, S.Z., Wan, Y.G., Huang, J.C., Bu, Y.F., Li, X., 2015. Present tectonic stress field in the
763 Circum-Ordos region deduced from composite focal mechanism method. Chin. J.
764 Geophys. 58(2), 436–452. <https://doi.org/10.6038/cjg20150208>.
- 765 Stephansson, O., Brown, E.T., 2015. Rock stress and rock stress measurements: a review. Eng.
766 Geol. 49(1), 81–82. [https://doi.org/10.1016/S0013-7952\(97\)85629-3](https://doi.org/10.1016/S0013-7952(97)85629-3).
- 767 Su, S.R., 2002. Influence of fault structure on in-situ stress field and its engineering application.
768 Science Press, Beijing. pp 15–68.
- 769 Sun, Z.Q., Zhang, J.H., 2004. Variation of in-situ stresses before and after occurrence of
770 geologic fault structure. Chin. J. Rock. Mech. Eng. 23, 3964–3969.
- 771 Townend, J., Zoback, M.D., 2000. How faulting keeps the crust strong. Geology. 28(5), 399–
772 402. [https://doi.org/10.1130/0091-7613\(2000\)28<399:hfkts>2.0.co;2](https://doi.org/10.1130/0091-7613(2000)28<399:hfkts>2.0.co;2).
- 773 Tuncay, E., Ulusay, R., 2008. Relation between Kaiser effect levels and pre-stresses applied in
774 the laboratory. Int. J. Rock. Mech. Min. Sci. 45(4), 524–537. <https://doi.org/10.1016/j.ijrmms.2007.07.013>.
- 775 Wang, C.H., 2014. Brief review and outlook of main estimate and measurement methods for
776 in-situ stress in rock mass. Geol. Rev. 60(5), 971–996. <https://doi.org/10.3969/j.issn.0371-5736.2014.05.003>.
- 777 Wang, L.L., Jiang, B., Wang, J.L., Qu, Z.H., 2018. Effects of in-situ stress and joint on
778 permeability of the coal bed in Linfen block, southeastern Ordos Basin, China. Russ. Geol.
779 Geophys., 59(3):299–312. <https://doi.org/10.1016/j.rgg.2018.03.008>.
- 780 Wang, S.M., Zhang, Y.P., 1999. Study on the formation, evolution and coal accumulating
781 regularity of the Jurassic Ordos Basin. Earth Science Frontiers. 6(S1), 147–155.
782 <https://doi.org/10.16509/j.georeview.2014.05.005>.
- 783 Wu, S., Tang, D.Z., Li, S., Wu, H.Y., Hu, X., Zhu, X.G., 2017. Effects of geological pressure
784 and temperature on permeability behaviors of middle-low volatile bituminous coals in
785 eastern Ordos Basin, China. J. Petrol. Sci. Eng., 153(5), 372–384.
786 <https://doi.org/10.1016/j.petrol.2017.03.034>.
- 787 Xiao, W., Lv, X.J., Zhao, Y.L., Sun, H.X., Li, J.Q., 2020. Ecological resilience assessment of
788 an arid coal mining area using index of entropy and linear weighted analysis: A case study
789 of Shendong Coalfield, China. Ecol. Indic., 109(2), 105843. <https://doi.org/10.1016/j.ecolind.2019.105843>.
- 790 Xie, H.P., Gao, F., Ju, Y., 2015. Research and exploration of deep rock mechanics. Chin. J.
791 Rock. Mech. Eng. 34(11), 2161–2178. <https://doi.org/10.15961/j.jsuese.201700025>.
- 792 Xie, Q., Qiu, P., Yu, X.B., Carlos, D.G., 2010. Initial-stress measurements with AE and DRA
793 combined technique. J. Chin. Coal. Soc. 35(4), 559–564. [https://doi.org/10.1016/S1876-3804\(11\)60004-9](https://doi.org/10.1016/S1876-3804(11)60004-9).
- 794 Yang, D.H., Zhao, Y.X., Zhang, C., Teng, T., He, X., Wang, W., Han, P.H., 2018. Experimental
795 study on the influence of cyclic loading on Kaiser effect of sedimentary rocks. Chin. J.
796 Rock. Mech. Eng. 37(12), 2697–2708. <https://doi.org/10.13722/j.cnki.jrme.2018.0394>.
- 797 Yang, F., Yang, X.C., Jiang, B., Zhou, K., Chen, C.H., 2014. Analysis on tectonic characteristics

- 802 and tectonic stress field in Baode area. Coal. Sci. Tech. 42(7), 92–97.
803 <https://doi.org/10.13199/j.cnki.cst.2014.07.024>.
- 804 Ye, F.W., Liu, D.C., Huang, X.F., Zhang, B.J., 2006. Study on fault tectonics in northern Ordos
805 Basin using Post remote sensing application technology. Uranium Geology. 22(3), 182–
806 189. <https://doi.org/10.1007/s11769-006-0026-1>.
- 807 Yoshikawa, S., Mogi, K., 1989. Experimental studies on the effect of stress history on acoustic
808 emission activity: A possibility for estimation of rock stress. J. A. E. 8, 113–123.
- 809 Yuan, L., 2017. Scientific conception of precision coal mining. J. Chin. Coal. Soc. 42(1), 1–7.
810 <https://doi.org/10.13225/j.cnki.jccs.2016.1661>.
- 811 Zang, A., Stephansson, O., 2013. Crustal stress field. Seismological Press, Beijing. pp 90–230.
- 812 Zhang, D.S., Ma, L.Q., Wang, X.F., Fan, G.W., 2009. Aquifer-protective mining technique and
813 its application in shallowly buried coal seams in Northwest of China. Procedia. Earth.
814 Planet. Sci., 1(9), 60–67. <https://doi.org/10.1016/j.proeps.2009.09.012>.
- 815 Zhang, H., Meng, Z.P., He, Z.L., 2000. Study on tectonic stress field in the Ordos coal basin.
816 J. Chin. Coal. Soc. 25(S1), 1–5. <https://doi.org/10.13225/j.cnki.jccs.2000.s1.002>.
- 817 Zhang, Y.Q., Shi, W., Liao, C.Z., Hu, B., 2006. Fault Kinematic Analysis and Change in Late
818 Mesozoic Tectonic Stress Regimes in the Peripheral Zones of the Ordos Basin, North
819 China. Acta Geologica Sinica. 80(5), 639–647. [https://doi.org/10.1016/S1001-8042\(06\)60011-0](https://doi.org/10.1016/S1001-8042(06)60011-0).
- 821 Zhao, J. L., Tang, D.Z., Lin, W.J., Qin, Y., Xu, H., 2019. In-situ stress distribution and its
822 influence on the coal reservoir permeability in the Hancheng area, eastern margin of the
823 Ordos Basin, China. J. Nat. Gas. Sci. Eng., 61(1), 119–132. <https://doi.org/10.1016/j.jngse.2018.09.002>.
- 825 Zhao, J.L., Tang, D.Z., Qin, Y., Xu, H., 2018. Experimental study on structural models of coal
826 macrolithotypes and its well logging responses in the Hancheng area, Ordos Basin, China.
827 J. Petrol. Sci. Eng., 166(8), 658–672. <https://doi.org/10.1016/j.petrol.2018.03.073>.
- 828 Zoback, M.D., 2007. Reservoir Geomechanics. Cambridge University Press, New York. pp 36–
829 110.

Figures

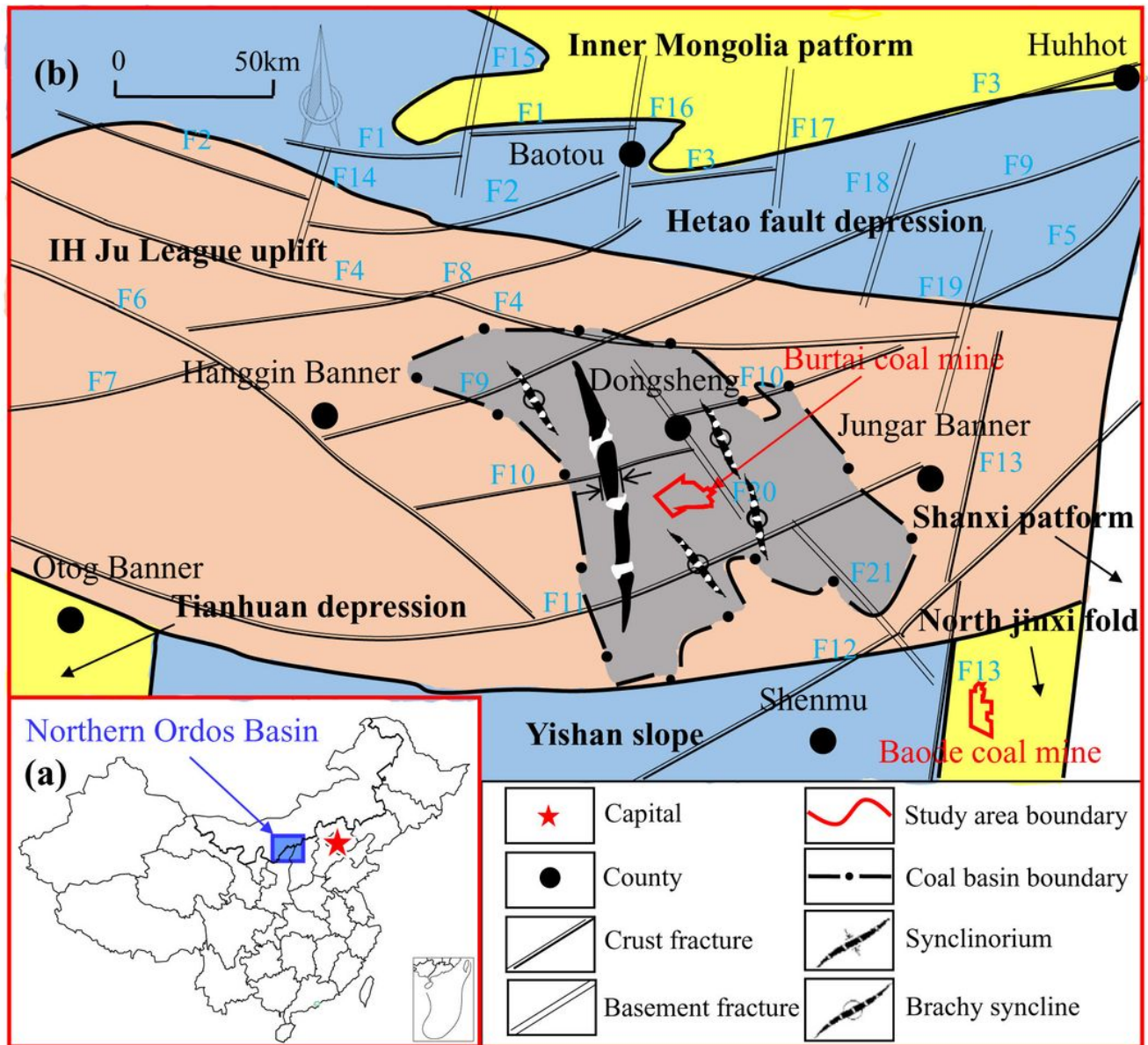


Figure 1

Regional tectonic outline of Burtai mine and Baode mine. (a), location of northern Ordos Basin (He, 2013); (b), tectonic distribution of northern Ordos Basin. Notes: F1, Ural mountain; F2, Hetao basin; F3, Daqing mountain; F4, Northern margin of Ordos Basin; F5, Horinger; F6, Hanggin banner-Ejin Horo banner; F7, Wuhai North; F8, Dalad banner; F9, Hanggin banner-Togtoh; F10, Ordos-Dongsheng; F11, Wuhai-Ejin Horo banner-Jungar banner; F12, Uxin banner-Shenmu-Fugu; F13, Linfen-Lishi-Pianguan; F14, Leap Hetao basin; F15, Leap Ural 7 mountain ; F16, Leap Ural mountain and Daqing mountain; F17, Leap Daqing mountain; F18, South Linhe; F19, Boundary between northern margin of Ordos Basin fault and Lingle fault; F20, East Dongsheng; F21, Leap near NE fault.

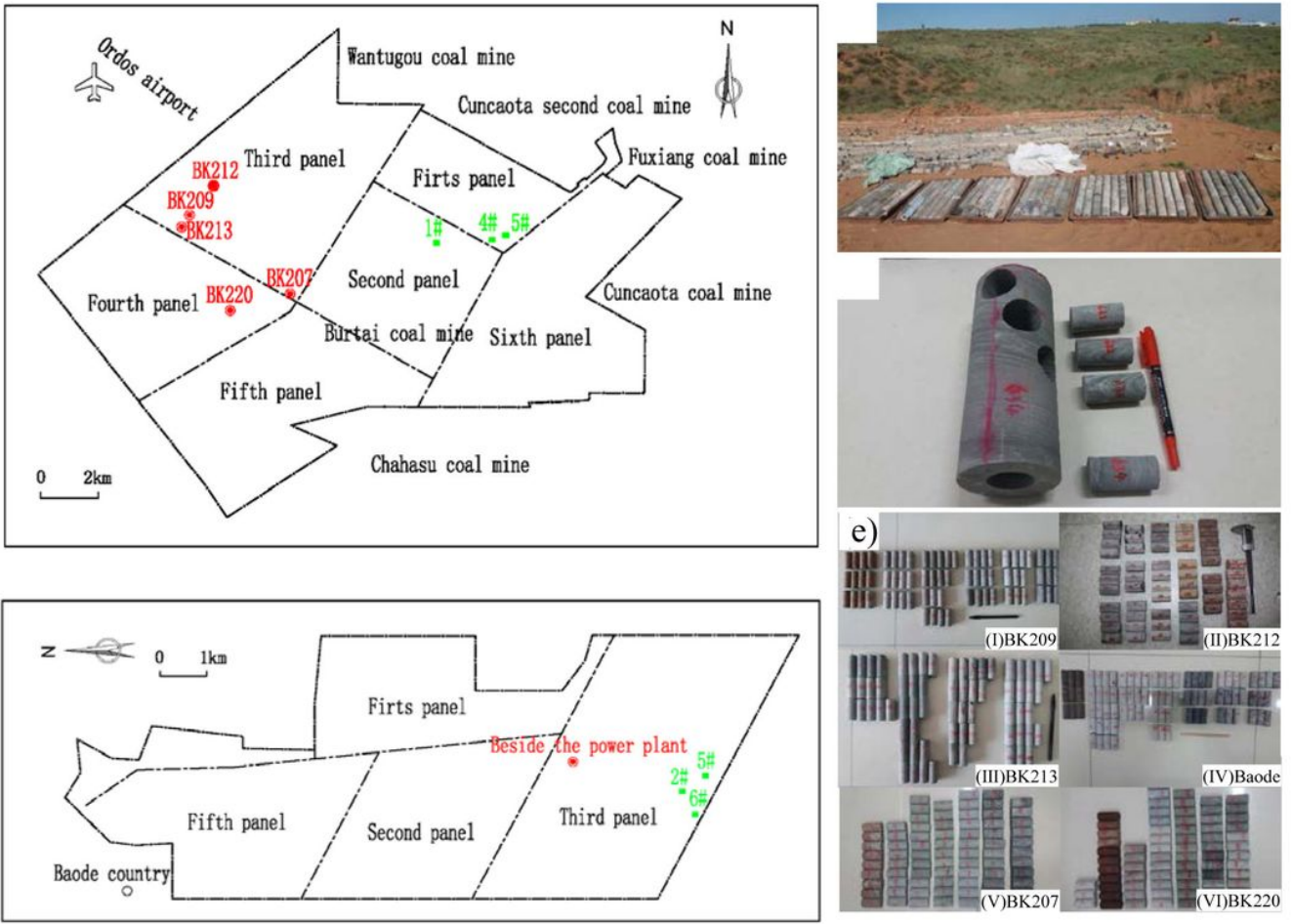


Figure 2

Coring and processing of the samples. (a), sampling location in Burtai mine; (b), sampling location in Baode mine; (c), on-site coring (BK220); (d), sampling from rock core; (e), processed samples. Notes: red, the core sampling location tested by AE; light green, the on-site test location by OC.

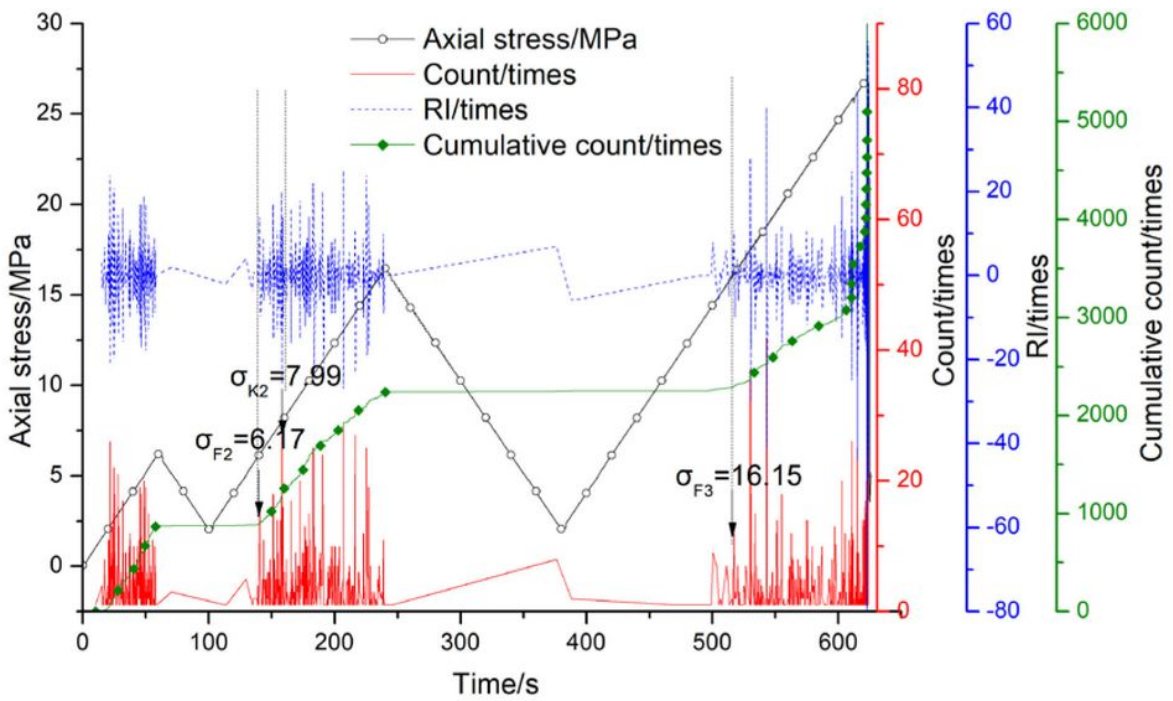


Figure 3

KE point recognition by AE during gradual increase cyclic loading. Notes: σ_{Fi} , the KE (BK209(BK213(BK212(BK220(BK207(e) point stress corresponding to σ_p in the i cycle; σ_{Ki} , the KE point stress corresponding to σ_{Hmax} in the i cycle.

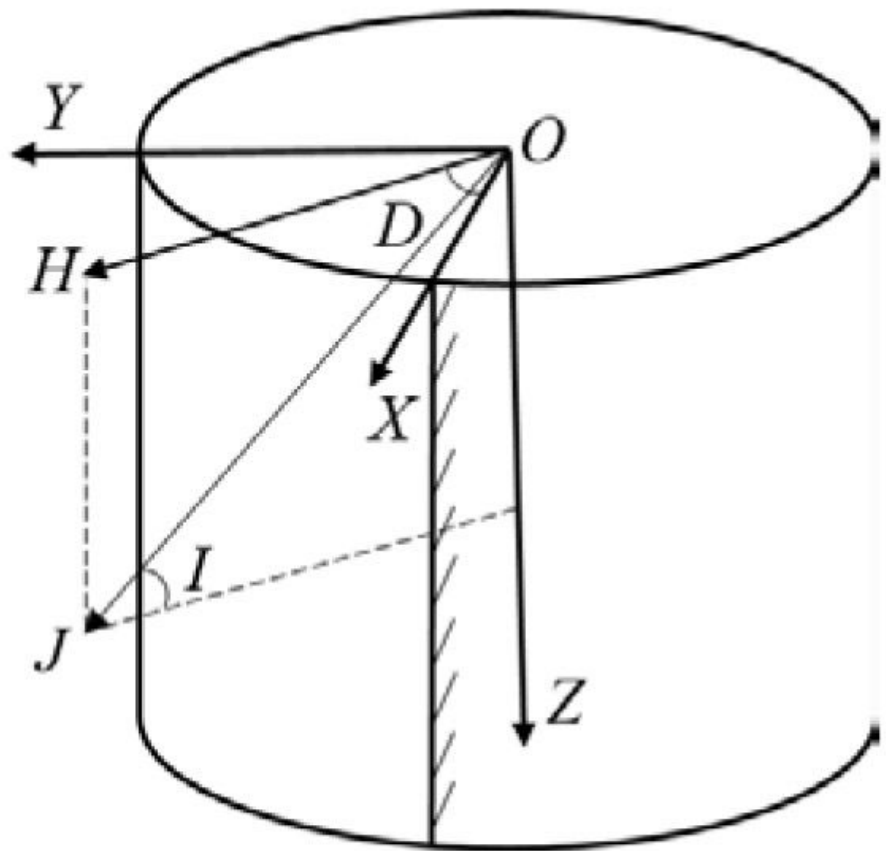


Figure 4

Schematic diagram of relative coordinate system on geomagnetic sample

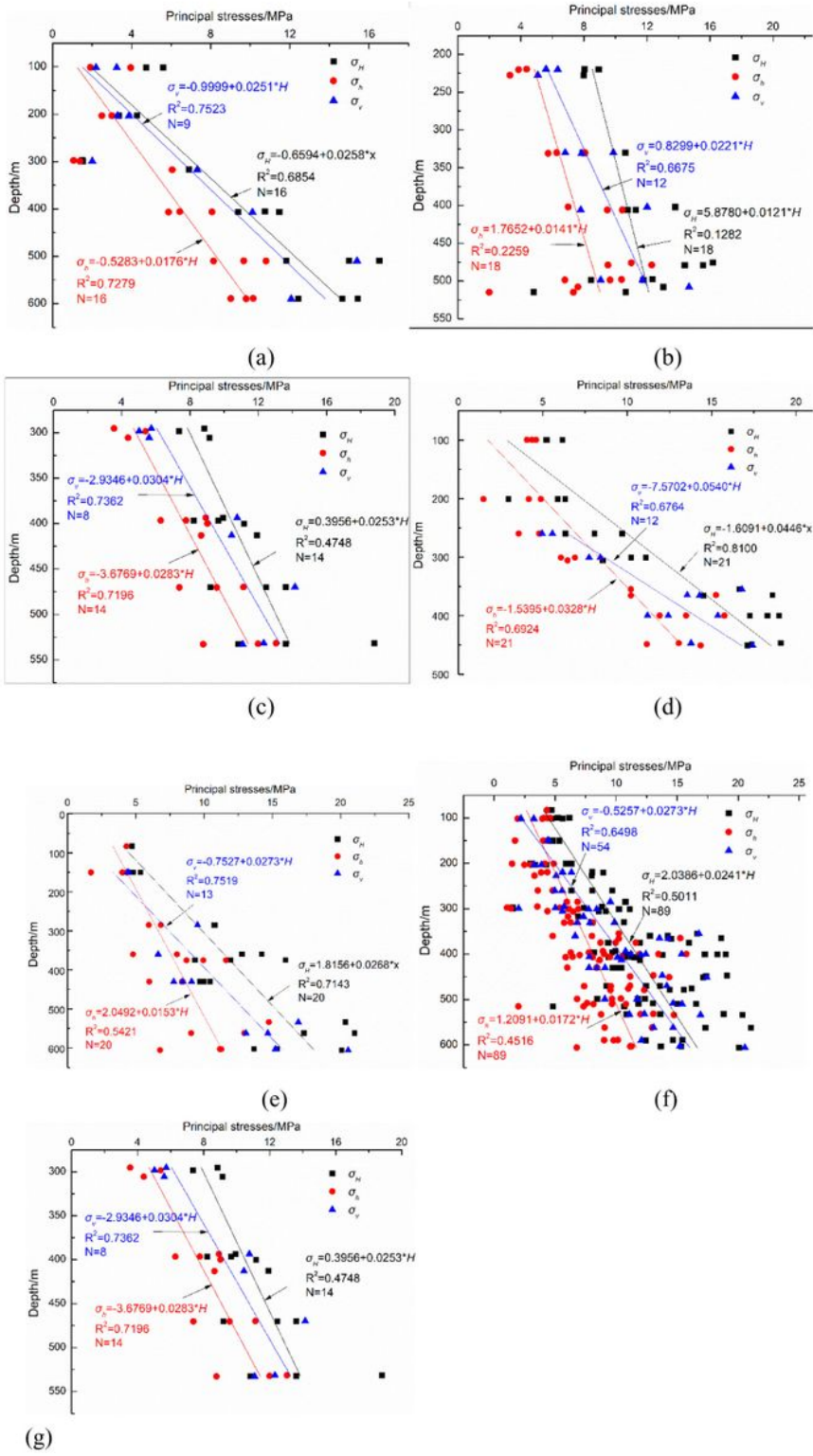


Figure 5

The relationship between σ_H , σ_h and σ_v vs. depth. (a), BK212; (b), BK209; (c), BK213; (d), BK207; (e), BK220; (f), σ_H , σ_h and σ_v vs. depth in Burtai mine; (g), σ_H , σ_h and σ_v vs. depth in Baode mine.

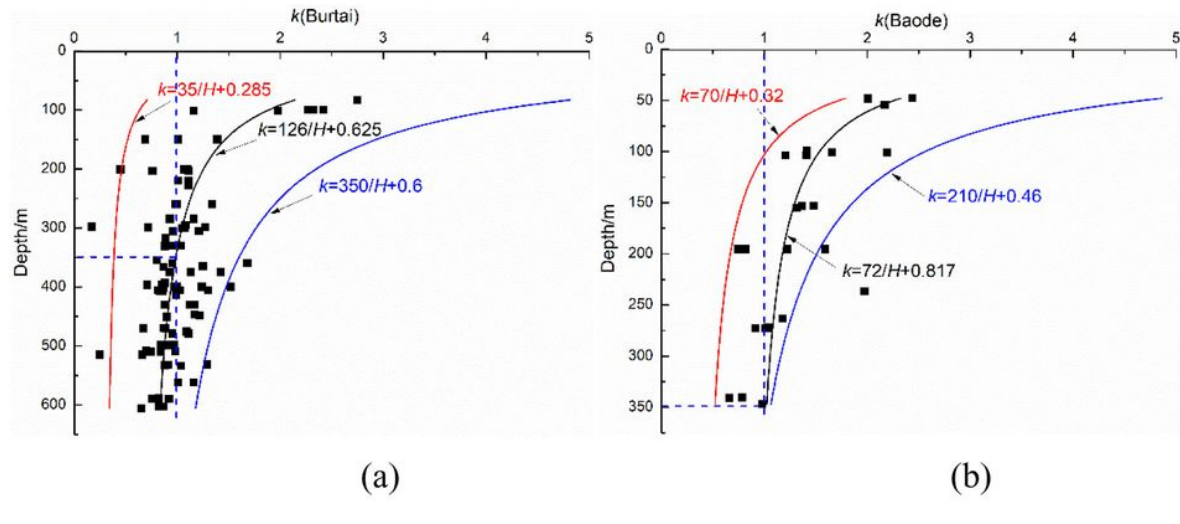


Figure 6

Scatter plot of k vs. depth and its relationship. (a), k vs. depth in Burtai mine; (b), k vs. depth in Baode mine.

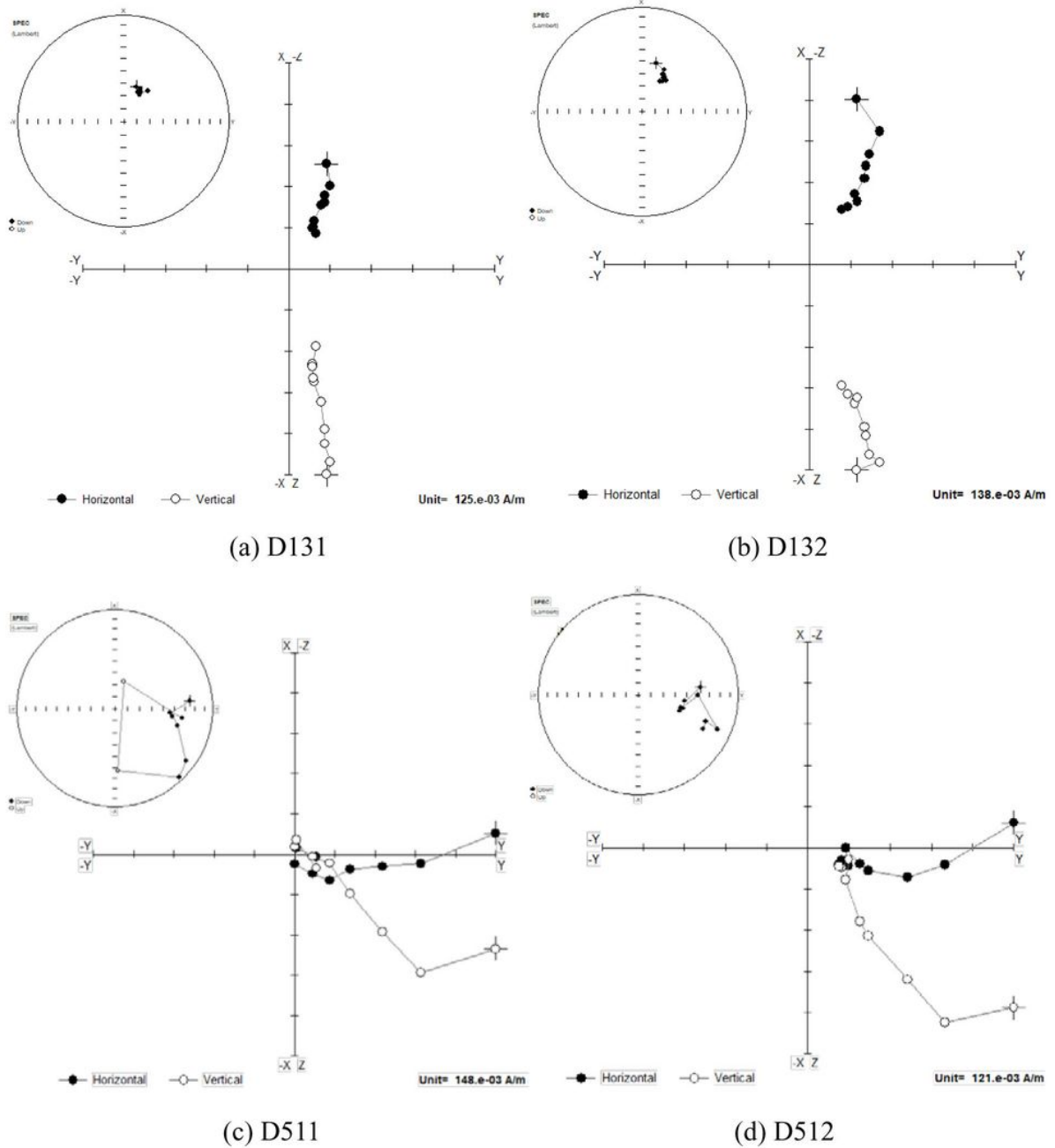
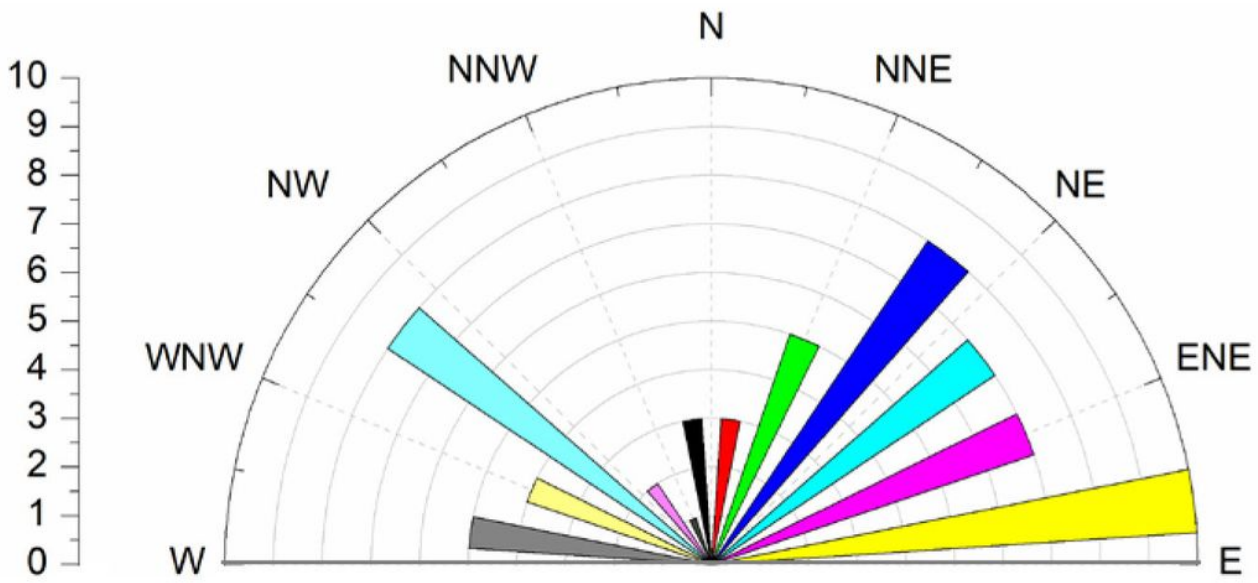
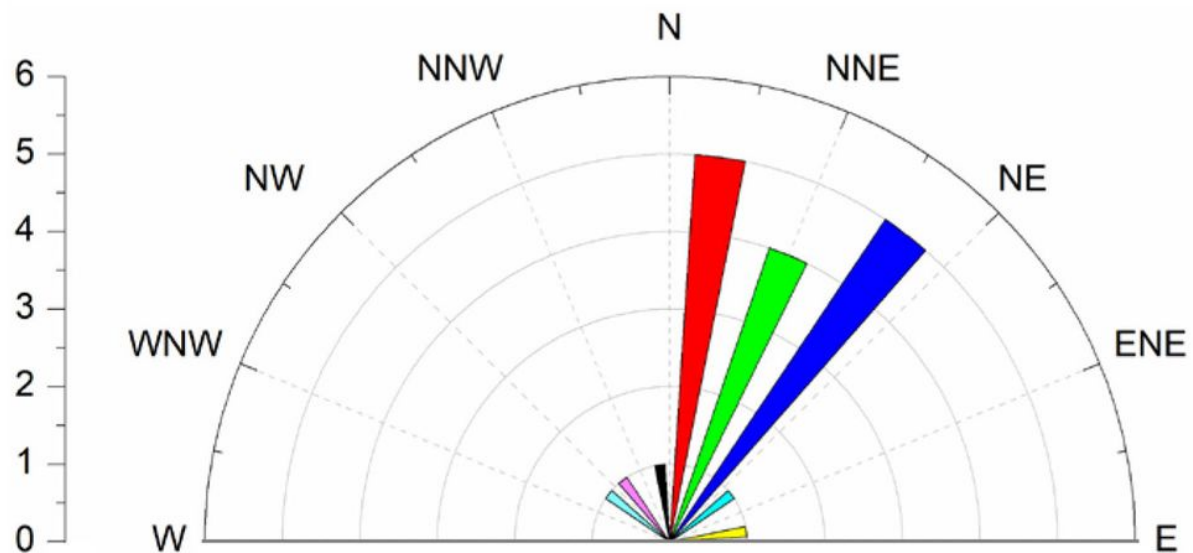


Figure 7

Thermal demagnetization curves of samples in BK207. (a), D131; (b), D132; (c), D511; (d), D512.



(a)



(b)

Figure 8

Half rose diagram of σH azimuth. (a), σH azimuth in Burtai mine; (b), σH azimuth in Baode mine.

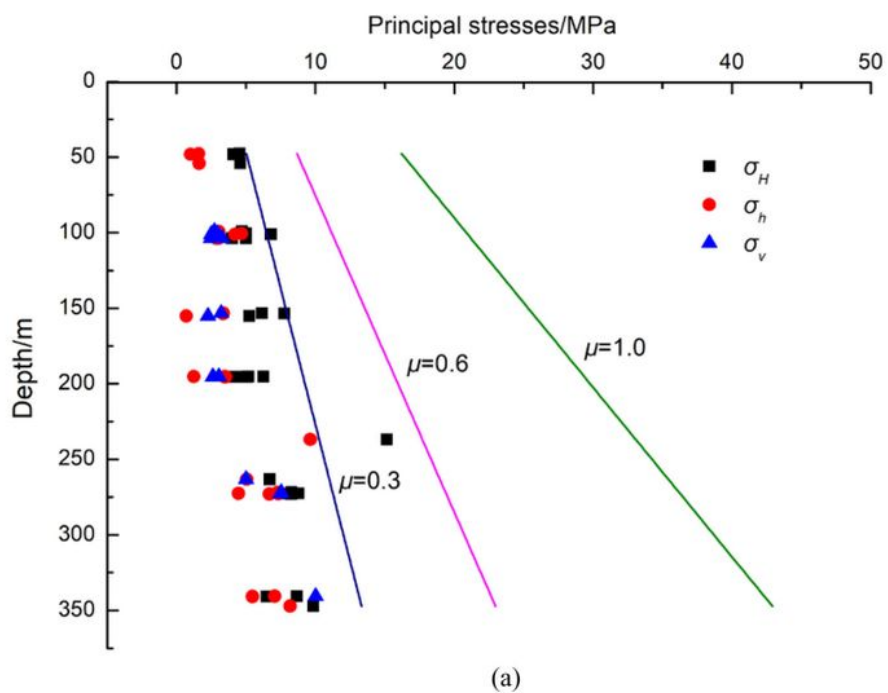
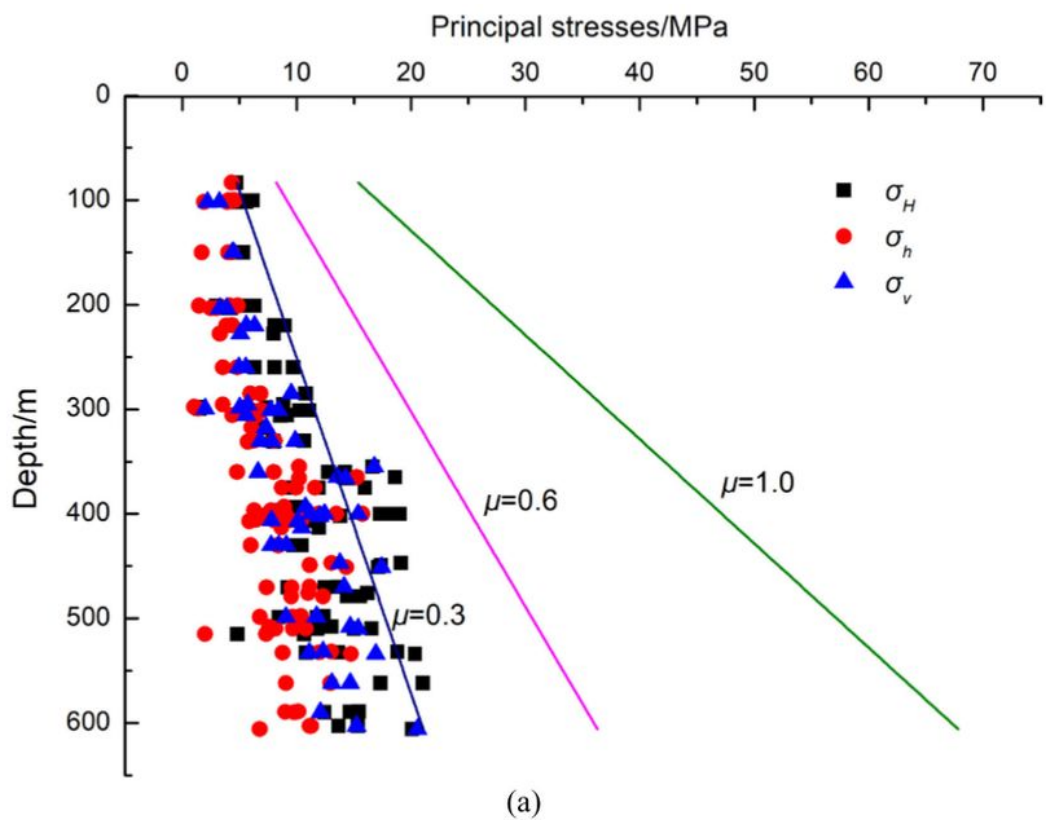


Figure 9

The relationship between principal stress vs. μ . (a), principal stress vs. μ in Burtai mine; (b), principal stress vs. μ in Baode mine.

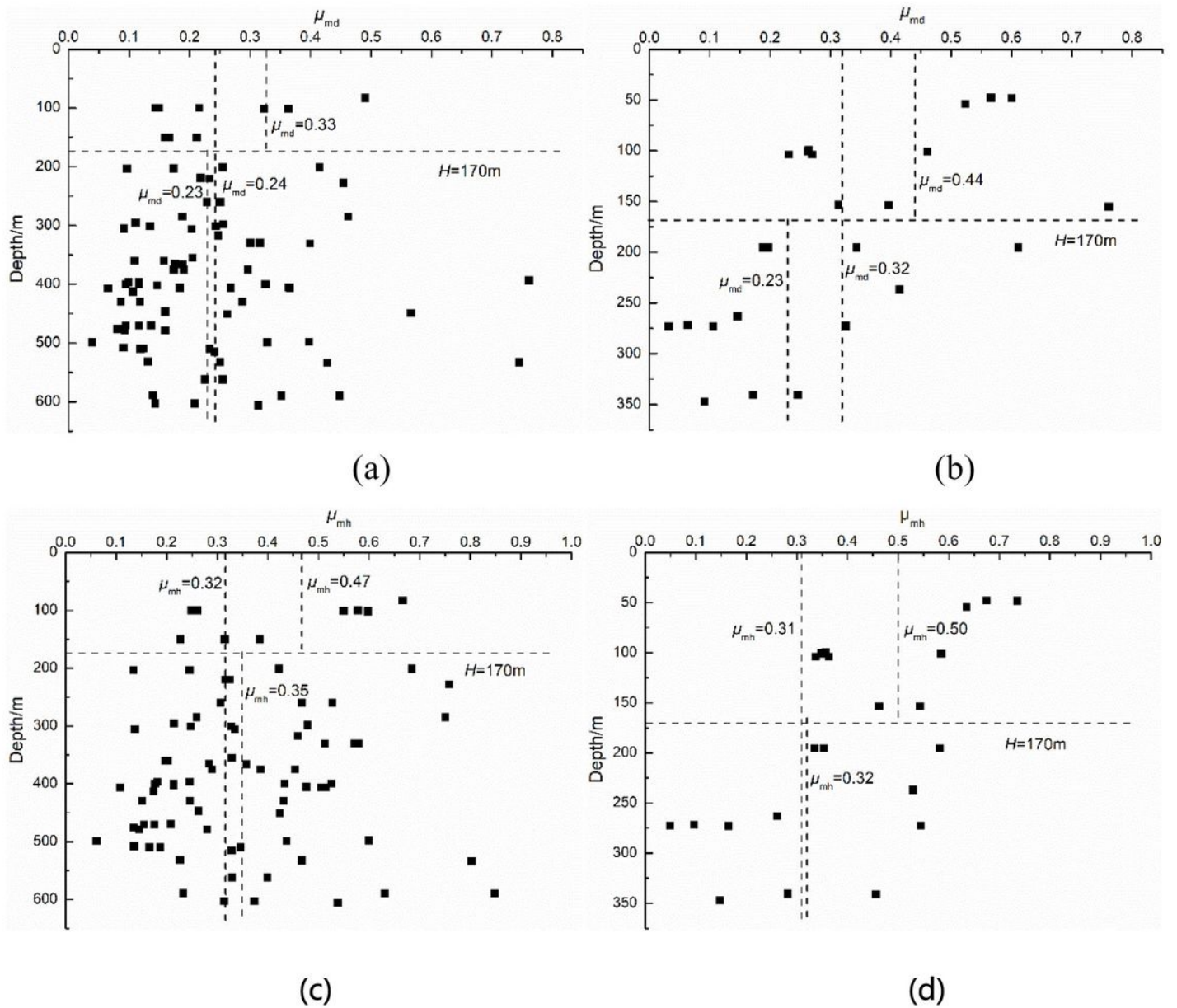


Figure 10

Scatter plot of μ_{md} and μ_{mh} vs. depth and its relationship. (a), μ_{md} vs. depth and its relationship in Burtai mine; (b), μ_{md} vs. depth and its relationship in Baode mine; (c), μ_{mh} vs. depth and its relationship in Burtai mine; (d), μ_{mh} vs. depth and its relationship in Baode mine.

Supplementary Files

This is a list of supplementary files associated with this preprint. Click to download.

- [Tables.pdf](#)
- [Insitu stress test results by AE.xls](#)